This manuscript is a non-peer-reviewed EarthArXiv preprint that has been submitted to the IEEE Journal of Selected Topics in Applied Earth Observations and Remote Sensing. Subsequent versions may contain slightly different content.

First Characterisation of P-band Scattering Mechanisms from Orbit in Lower Shire Valley, southern Malawi, using ESA Biomass Imagery

Clinton Nkolokosa., *Student Member IEEE,* Olivier D'Hondt, Lucio Mascolo, *Member IEEE,* Tiwonge Mzumara-Gawa, Petros Chigwechokha, Russell Stothard, Zarah Pattison, Armando Marino., *Fellow, IEEE*

***Abstract*—The European Space Agency (ESA) Biomass mission provides the first spaceborne fully polarimetric P-band synthetic aperture radar (SAR) observations in orbit. Here, we report the first characterisation of P-band scattering mechanisms over the Lower Shire Valley (LSV) floodplain, southern Malawi. A single quad-polarimetric acquisition, collected at the onset of the rainy season in November 2025, was subjected to eigenvector-eigenvalue decomposition (entropy *H*, anisotropy *A*, and mean alpha angle $\bar{\alpha}$), alongside radar vegetation index, model-based Van Zyl and Yamaguchi four-component decompositions. Across the study area, surface scattering constitutes the dominant backscatter mechanism, reflecting both the prevalence of bare soil within the landscape and the capacity of P-band wavelength to penetrate vegetation canopies and interact with the underlying surface. Volume scattering represents the second most significant contribution, associated with forested areas, shrubland, hectare-scale cropland, and dense wetland vegetation. Double-bounce returns are the least prevalent, confined principally to the built-up area. Of the polarimetric parameters examined, $\bar{\alpha}$ emerges as the most diagnostic for discriminating bareland from vegetation classes. However, no single parameter fully resolves all vegetation cover types in isolation, though *H* shows potential in this regard. These results furnish a physical baseline for future Biomass acquisitions over the LSV. As such, this work serves as a primer for the retrieval of key vegetation, water and soil parameters, such as surface soil moisture, sub-canopy flood inundation, and aboveground biomass.**

***Index Terms*—ESA Biomass mission, Malawi, polarimetry SAR, P-band, PyPolSARpro, vegetation**

I. INTRODUCTION

Applications of synthetic aperture radar (SAR) in monitoring the Earth's surface have firmly substantiated the utility and value of microwave remote sensing in addressing key global challenges, ranging from floods and droughts [1], [2], deforestation [3], and carbon stock accounting [4], to glacier dynamics [5] and landslide detection [6]. Central to these applications is the retrieval of geo- and bio-physical parameters that quantify the state and rate of change of critical natural resources (water, forest and land). Collectively, these parameters underpin the water and carbon cycles that shape global environmental and climatic processes. Of note, the ecosystem services provided by these resources are estimated to be worth $125–$140 trillion per year globally [7]. In Africa, their degradation is costing the continent an estimated $7-$15 billion annually [8]. This underscores the immense societal and economic stakes of monitoring them effectively. Yet with increasing losses and persistent data gaps [9], this remains a pertinent challenge in addressing both natural and anthropogenic catastrophe perils resulting from unsustainable extraction and exploitation. Critically, SAR signals penetrate clouds and, depending on wavelength, a certain thickness of vegetation and soil. In the context of vegetated environments, this makes SAR imaging a uniquely capable and reliable tool for estimating surface inundation extent, height, density and above ground biomass of vegetation stands, and surface soil moisture regardless of cloud cover, haze, or darkness [10]. Accordingly, X (10.7GHz), C- (6.9GHz) and L- (1.4 GHz) band SAR systems have underpinned global monitoring datasets, in tandem with optical data (e.g., multispectral imagery). For example, C-band sensors (e.g., from ENVISAT ASAR to the current Sentinel-1 constellation) have been widely used to narrow the environmental data gap (e.g., coverage, granularity, quality and accessibility). An examplar is the retrieval of surface backscatter and the subsequent mapping of inundation extent in open and sparsely vegetated wetlands [11], [12]. L-band systems, particularly JERS-1 and ALOS PALSAR, extended this capability into denser vegetation by exploiting the double-

· This work was funded by the Commonwealth Scholarship Commission and the Foreign, Commonwealth and Development Office in the UK. All views expressed here are those of the author(s) not the funding body. *(Corresponding author: Clinton Nkolokosa)*

Clinton Nkolokosa is with the University of Stirling, Stirling FK9 4LA, UK (email: clinton.nkolokosa@stir.ac.uk)

Olivier D'Hondt is with SAREO, Poland (email: dhondt.olivier@gmail.com).

Lucio Mascolo is with the Radarmetrics, Spain (email: lucio.mascolo@gmail.com)

Tiwonge Mzumara-Gawa is with the Malawi University of Science and Technology, Thyolo, Malawi (email: tgawa@must.ac.mw)

Petros Chigwechokha is with the Malawi University of Science and Technology, Thyolo, Malawi (email: pchigwechokha@must.ac.mw)

Russell Stothard is with the Liverpool School of Tropical Medicine, Liverpool L3 5QA, UK (email: russell.stothard@lstmed.ac.uk)

Zarah Pattison is with the University of Stirling, Stirling FK9 4LA, UK (email: zarah.pattison2@stir.ac.uk)

Armando Marino is with the University of Stirling, Stirling FK9 4LA, UK (email: armando.marino@stir.ac.uk)

This manuscript is a non-peer-reviewed EarthArXiv preprint that has been submitted to the IEEE Journal of Selected Topics in Applied Earth Observations and Remote Sensing. Subsequent versions may contain slightly different content.

bounce interaction between flooded trunks and the water surface [13], [14]. This enabled the discrimination of flooded forest, emergent vegetation, and open water across tropical and boreal floodplains. There is a principal limitation, however. Based on radiative transfer theory (i.e., wave propagation through a medium) [15], shorter wavelengths tend to experience increased vegetation attenuation [16]. Longer wavelengths, conversely, afford deeper penetration into the canopy. Various studies have assessed SAR sensitivity to elements of tree structure (leaves, branches, and trunks) and canopy penetration efficacy as a function of wavelength [17], [18]. Such studies consistently show that the shorter the wavelength, the more rapid the signal saturation and the weaker the penetration, and vice versa. This postulates that considerably longer wavelengths (namely, P-band) hold the potential to address current challenges in the retrieval of accurate surface water, soil and forest parameters, including indicators of anthropogenic disturbance, in densely vegetated areas; potentially enabling superior estimation. The unprecedented availability of spaceborne P-band SAR observations from the Biomass mission (launched in April 2025) now presents the first opportunity to examine terrestrial processes at wavelengths previously inaccessible to satellite Earth observation. As the first European Space Agency (ESA) P-band satellite in low Earth orbit, Biomass operates at 435 MHz with fully polarimetric capabilities (i.e., coherent HH, HV, VV, VH channels measurement) [19]. The present study applies polarimetric decomposition approaches to Biomass imagery of the Lower Shire Valley (LSV) floodplain in Malawi to characterise P-band scattering mechanisms for the first time over this landscape. Of note, LSV is an extension of the East African Rift Valley and no previous study using P-band SAR have been conducted here. Against this background, we ask which observable scattering mechanisms dominate P-band Biomass imagery across the LSV, as revealed by a single acquisition collected at the onset of the rainy season. Given the novelty of the data, characterising P-band scattering mechanisms is key to understanding how longer-wavelength SAR signals interact with forests, wetlands and croplands. This is fundamental to realising the full potential of Biomass data.

II. Methodology

The analysis proceeds in six stages. First, the Pauli decomposition is applied to provide an initial characterisation of dominant scattering mechanisms across the scene. Second, the coherence between HV and VH channels is examined to assess the noise floor of the data. Third, full-pol measurements in the circular right (R)-circular left (L) basis are emulated, and the coherence between right and left circular polarisations is evaluated to investigate target orientation effects. Fourth, the three-component Van Zyl decomposition is applied to separate surface, double-bounce and volume scattering contributions using a model-based covariance matrix approach. Fifth, the four-component Yamaguchi (Y4R) decomposition extends this framework by additionally isolating helix scattering, accounting for the depolarising effects of complex and heterogeneous targets. Sixth, radar vegetation index (RVI) is calculated to map vegetated and non-vegetated areas. Finally, to extend our knowledge on this new data, eigenvector-eigenvalue polarimetric descriptors, namely entropy H, anisotropy A and mean alpha angle $\bar{\alpha}$ (H/A/$\bar{\alpha}$), are characterised and visualised. These analyses are implemented using PyPolSARpro [20].

A. Study area

The LSV floodplain is in southern Malawi (Fig. 1). The landscape is characterised by seasonally inundated wetlands, riparian woodlands, and extensive herbaceous cover. This makes it well-suited for an initial exploratory analysis of P-band scattering. The district of Chikwawa, which encompasses the study area, retains substantial vegetation cover. In 2020 greater than 30 % tree cover was recorded, with natural forest accounting for 81 % (130 kha), followed by grassland at 16 % (27 kha), settlements at 2.0 % (3.6 kha), cropland at 0.61 % (1.0 kha), wetlands (dambo) at 0.12 % (200 ha), and other land covers comprising less than 0.1 % (43 ha) [21].

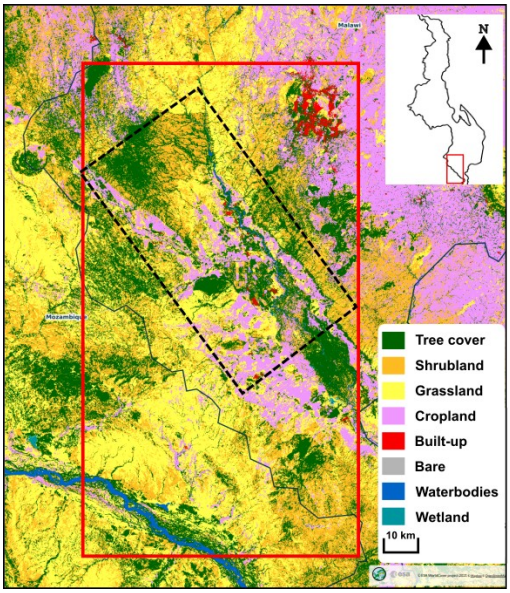

Fig. 1. Land cover across study area (dotted black line) in 2021 [22].

B. Dataset

This study uses early-access P-band SAR data from the ESA Biomass Earth Explorer 7 mission (hereafter Biomass). In contrast to conventional C- and L-band systems (e.g., Sentinel-1 5.6 cm wavelength, SAOCOM 23.5 cm wavelength), the considerably longer P-band wavelength (~70 cm) affords enhanced penetration through vegetation canopies and shallow surface layers. This confers sensitivity to sub-canopy structure, inundated ground surfaces, and complex vegetation–water interactions [19]. Capitalising on these

This manuscript is a non-peer-reviewed EarthArXiv preprint that has been submitted to the IEEE Journal of Selected Topics in Applied Earth Observations and Remote Sensing. Subsequent versions may contain slightly different content.

physical properties, the Biomass mission is designed to measure forest height and structure, estimate above ground biomass and forest height, map forest floor topography, soil surface measurements, and characterize ice-sheet structure [23]. Collectively, these observations will address critical gaps, both in data and understanding, within the forest–carbon–climate nexus. The dataset comprises Level-1 Single-look Complex Slant-range (SCS) products acquired in quad-polarimetric mode (HH, HV, VH, VV) during the tomographic mission phase. These data preserve fully calibrated amplitude and phase information suitable for polarimetric decomposition. Data were downloaded from the ESA Multi-mission Algorithm and Analysis Platform (MAAP) (https://explorer.maap.eo.esa.int/?q=BiomassLevel1a), preprocessed through the Biomass processing chain, including antenna pattern correction, radio-frequency interference suppression, and first-order ionospheric compensation [19]. Following the satellite launch on 29 April 2025, the Biomass archive commenced on 21 November 2025 (Fig. 2). The acquisition analysed here was collected on 24 November 2025 at the onset of the rainy season over the LSV. The original scene encompasses the LSV floodplain and surrounding escarpments, including portions of Blantyre City, and the Zambezi River. For this analysis, the scene was spatially subset to the defined study area prior to processing. Full technical specifications are provided in Table 1.

TABLE I
TECHNICAL SPECIFICATIONS OF THE BIOMASS P-SAR DATASET.

Parameter	Description
Product identifier	BIO_S1_SCS__1S_20251124T154220_20251124T154241_T_G01_M01_C02_T010_F169_01_DK5V2B
Processing level	Level-1A (SLC Slant-range)
Instrument	P-band SAR
Center frequency	435 MHz, 70 cm wavelength
Operational mode	SM (Stripmap)
Polarisation mode	Quad-pol (HH, HV, VH, VV)
Instrument type	Imaging microwave radars
Orbit number	3070
Orbit direction	Descending
Antenna look direction	Left-looking
Mission phase	Tomographic
Near incidence angle	>23°
Acquisition time (UTC)	24 Nov 2025, 15:42:20–15:42:41
Data format (size)	GeoTIFF (504.0 MB)
Processor version	4.2.2
Processing mode	Operational
Geographic footprint	34.28–35.14°E, 15.62–16.88°S

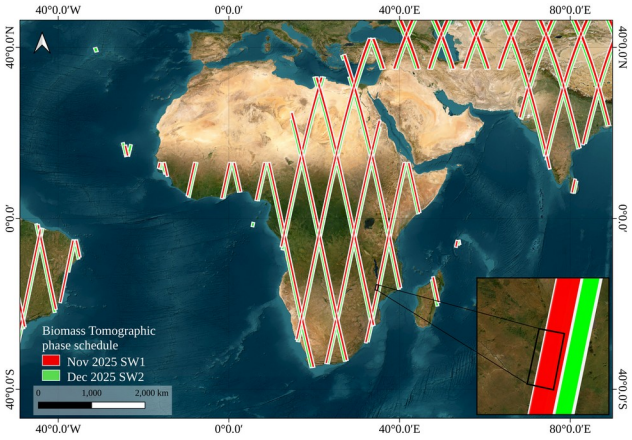

Fig. 2. The initial schedule for the tomographic phase for Biomass mission for major cycle 1 in late 2025, with a focus on study area.

B. Software

In this analysis, we used PyPolSARpro [20], a Python-based re-implementation of selected core components of the PolSARpro toolbox, designed to provide a more accessible and reproducible environment for polarimetric SAR data processing. PyPolSARpro was chosen because of its accessibility, following recent community recommendations to modernize PolSARpro (originally developed in C with a graphical user interface) by adopting a flexible, programmatic approach that facilitates automation, reproducible workflows, and integration into larger processing pipelines. A further advantage is that it is built upon Xarray with a Dask backend, enabling the handling of labeled multi-dimensional data and scalable computation. This allows polarimetric matrices (e.g., S, C_3, T_3, T_4) to be represented as structured datasets with explicit metadata, while lazy evaluation and parallel task scheduling enable efficient processing of large datasets without requiring explicit memory management or tiling strategies. Although the software supports input data in the NetCDF-BEAM format used by SNAP, its underlying data model is designed to be extensible, allowing custom import functions to be implemented with minimal effort. This flexibility facilitates integration with platforms such as MAAP and enables the ingestion of emerging datasets, including Biomass products.

PyPolSARpro is open-source (Apache-2.0) and distributed via the conda-forge channel, making installation straightforward across platforms. The current implementation includes commonly used polarimetric filters and decompositions, such as Boxcar and Refined Lee filtering, Van Zyl, Freeman-Durden, and Yamaguchi (three- and four-component) decompositions, as well as the Polarimetric Whitening Filter. Validation on real quad-polarimetric ALOS-1 data demonstrates strong numerical agreement with the original

This manuscript is a non-peer-reviewed EarthArXiv preprint that has been submitted to the IEEE Journal of Selected Topics in Applied Earth Observations and Remote Sensing. Subsequent versions may contain slightly different content.

PolSARpro routines, while ongoing developments aim to extend the range of available methods [20]. To our knowledge, this study represents one of the first applications of PyPolSARpro to Biomass P-band data, serving as an early demonstration.

C. Polarimetric decomposition

Three complementary decomposition methods were applied in this study. One, the eigenvalue decomposition H/A/$\bar{\alpha}$ also known as Cloude-Pottier decomposition [24]. Two, the Van Zyl three-component model [25]. Three, the Yamaguchi 4-component Y4R model [26]. The advantage of this multi-procedure is threefold. First, the eigenvalue and model-based (Van Zyl, Y4R) decompositions describe scattering mechanisms from fundamentally distinct theoretical standpoints. The former characterizes the statistical structure and randomness of the coherency matrix in a basis-invariant manner [24]. The latter partitions total backscattered power into physically based canonical scattering mechanisms under explicit structural assumptions [27]. In the context of Biomass P-band data, such dual characterization is particularly pertinent, as the long wavelength enhances penetration and complex volume–ground interactions whose relative contributions are yet to be fully empirically resolved. For instance, in a heterogeneous floodplain comprising mixed forest, wetland, cropland, and shrubland, as exemplified in our study area, P-band returns could plausibly arise from tree canopies, wetland or partially submerged vegetation, and bare soil.

For the purpose of analysis, complex-valued scattering coefficients were reconstructed from the Biomass amplitude and phase GeoTIFF files using Euler's formula:

$$S_{ij} = |S_{ij}| e^{j\phi} \tag{1}$$

where $|S_{ij}|$ the amplitude and the phase for each polarization channel (HH, HV, VH, VV).

1. Pauli decomposition

Assuming the backscattering reciprocity condition $S_{HV} = S_{VH}$, the Pauli scattering vector was formed as:

$$k = \frac{1}{\sqrt{2}} \begin{bmatrix} S_{HH} + S_{VV} \\ S_{HH} - S_{VV} \\ 2S_{HV} \end{bmatrix} \tag{2}$$

The total backscattered power (Span) was computed as:

$$Span = |S_{HH}|^2 + |S_{VV}|^2 + 2|S_{HV}|^2 \tag{3}$$

and provides a polarisation-independent measure of scene backscatter intensity used as a reference for land cover discrimination [28].

The Pauli basis expresses the scattering matrix S as a linear combination of three canonical scattering matrices $\{\boldsymbol{S}_a, \boldsymbol{S}_b, \boldsymbol{S}_c\}$, with corresponding complex coefficients $\{a, b, c\}$ [28]:

$$a = \frac{(S_{HH} + S_{VV})}{\sqrt{2}} \tag{4a}$$

$$b = \frac{(S_{HH} - S_{VV})}{\sqrt{2}} \tag{4b}$$

$$c = \sqrt{2} S_{HV} \tag{4c}$$

Of note, the lexicographic representation of S in terms of $|\boldsymbol{S}_{HH}|^2$, $|\boldsymbol{S}_{VV}|^2$ and $2|\boldsymbol{S}_{HV}|^2$ lacks direct physical interpretation. The Pauli basis is preferred here because its coefficients correspond directly to canonical scattering mechanisms. $|a|^2$ is the power scattered by targets characterised by single- or odd-bounce scattering (sphere, plate, trihedral). $|b|^2$ is is the power scattered by targets characterised by double- or even-bounce scattering (dihedral at 0°). $|c|^2$ is the power returned on the orthogonal polarisation, associated with volume scattering such as that produced by the forest canopy [28]. Accordingly, the scene was visualised as an RGB composite (blue = $|a|^2$, single-bounce; red = $|b|^2$, double-bounce; green = $|c|^2$, volume scattering), following the standard codification of [28]. Multilooking (spatial averaging) and Refined Lee speckle filter were applied to reduce the (multiplicative) speckle noise inherent in SAR imagery. The T_3 matrix was then derived using the PyPolSARpro function S_to_T3() [20], [29].

2. Coherence between cross-polarization channels HV and VH

The coherence between the HV and VH cross-polarisation channels was examined to assess the noise floor of the Biomass SAR data. These two channels should be highly coherent under ideal, noise-free conditions, as the backscattering reciprocity conditions $S_{HV} = S_{VH}$ holds in a monostatic system [16]. Canonical targets such as trihedral and dihedral corner reflectors generate no cross-polarisation components (HV = VH = 0), providing a theoretical baseline against which channel consistency can be assessed [30]. In practice, however, the HV-VH correlation coefficient varies with target stationarity. For example, buildings maintain high correlation. Departures from the expected high correlation are therefore indicative of residual system noise, channel imbalance, or calibration errors [16], [33]. Critically, pixels

This manuscript is a non-peer-reviewed EarthArXiv preprint that has been submitted to the IEEE Journal of Selected Topics in Applied Earth Observations and Remote Sensing. Subsequent versions may contain slightly different content.

where $|\gamma_{HVVH}|$ is low identify locations where the cross-polarisation signal is unreliable and should be treated with caution in subsequent decomposition analyses. The complex coherence was estimated using a multilook boxcar estimator of the form:

$$\gamma = \frac{\langle S_{HV} \cdot S_{VH}^{*} \rangle}{\sqrt{\langle |S_{HV}|^2 \rangle \cdot \langle |S_{VH}|^2 \rangle}} \tag{5}$$

where angle brackets $\langle \ldots \rangle$ denote spatial averaging over the analysis window, and * denotes the complex conjugate [31], [32]. Both coherence magnitude, ranging from 0 (no coherence) to 1 (perfect coherence), and phase were computed. For a reciprocal medium the phase is expected to be near 0°, confirming that HV and VH measure the same physical interaction. By contrast, any departure would indicate phase offset, pointing to a processing artefact or antenna cross-talk [31].

3. Coherence between right and left circular polarization channels

The coherence between the right circular (RR) and left circular (LL) co-polarised channels was evaluated to investigate target orientation effects across the scene. Following [31] and [29], RR and LL were derived from the linear-basis scattering matrix under the BSA monostatic convention as

$$RR = \left(S_{HH} - S_{VV} + i2S_{HV}\right)/2 \tag{6a}$$

$$LL = \left(S_{VV} - S_{HH} + i2S_{HV}\right)/2 \tag{6b}$$

Here, both coherence magnitude $|\gamma_{RRLL}|$ and phase $\angle\gamma_{RRLL}$ were computed. The magnitude measures scattering determinism. Low values indicate depolarisation by volume scattering, while higher values indicate deterministic returns [29]. The phase is related to the dominant scatterer orientation angle θ via $\tan(4\theta)$, with values near 0° or 180° corresponding to horizontally or vertically oriented targets [31], [29]. A large phase standard deviation, by contrast, reflects scattering randomness, physically expected over depolarising vegetation. Asymmetry between RR and LL is indicative of oriented or helical scatterers that violate reflection symmetry. As a preliminary check, the Pearson correlation coefficient between and amplitudes was also computed.

4. Van Zyl decomposition

The Van Zyl three-component decomposition [25] was applied to separate the total backscattered power into three canonical scattering mechanisms: (1) odd-bounce (surface) scattering, representing direct reflection from surfaces; (2) double-bounce scattering, characteristic of vertical structures and dihedral reflectors; and (3) volume scattering contributions, arising from randomly oriented scatterers (here, vegetation). The Van Zyl decomposition separates total backscattered power into odd-bounce, double-bounce, and volume scattering contributions (Van Zyl, 1989). Here, the corresponding averaged covariance matrix C_3 can be expressed as

$$C_3 = \begin{bmatrix} \langle |S_{HH}|^2 \rangle & 0 & \langle S_{HH} S_{HV}^{*} \rangle \\ 0 & \langle |S_{HV}|^2 \rangle & 0 \\ \langle S_{HH} S_{HV}^{*} \rangle & 0 & \langle |S_{VV}|^2 \rangle \end{bmatrix} \tag{7}$$

5. Yamaguchi decomposition

The Y4R decomposition extends the Van Zyl approach by incorporating an additional helix scattering component to account for complex scattering from oriented vegetation and man-made structures [27]. This method decomposes the C_3 matrix into four components: (1) surface scattering; (2) double-bounce scattering; (3) volume scattering; and (4) helix scattering [26].

$$C_3 = f_s C_s + f_d C_d + f_v C_v + f_h C_h \tag{8}$$

where f_s, f_d, f_v and f_h, represent the powers of surface,double-bounce, volume and helix components, respectively [26]. The corresponding scattering powers are given by:

$$P_s = f_s\left(1 + |\beta^2|\right) \tag{9a}$$

$$P_d = f_d\left(1 + |\alpha^2|\right) \tag{9b}$$

$$P_v = f_v \tag{9c}$$

$$P_h = f_h \tag{9d}$$

where P_s, P_d, P_v and P_h are surface, double-bounce, volume, and helix power contributions to the Span, respectively (Yamaguchi et al., 2005). A detailed description of this decomposition approach is provided in [28]. Individual component maps, RGB composite visualizations (with red = double-bounce, green = volume, blue = surface/odd). In addition, histograms were generated for qualitative and quantitative analysis of the decomposition results.

6. H/A/$\bar{\alpha}$ decomposition and classification

The H/A/$\bar{\alpha}$ decomposition was applied to extract polarimetric descriptors from the T_3. This has the utility in

This manuscript is a non-peer-reviewed EarthArXiv preprint that has been submitted to the IEEE Journal of Selected Topics in Applied Earth Observations and Remote Sensing. Subsequent versions may contain slightly different content.

characterizing the randomness and nature of the scattering process. H/A/$\bar{\alpha}$ are defined as

$$H = -\sum_{i=1}^{3} p_i \log_3(p_i) \qquad p_i = \frac{\lambda_i}{\sum_{k=1}^{3} \lambda_k} \tag{10a}$$

$$A = \frac{(\lambda_2 - \lambda_3)}{(\lambda_2 + \lambda_3)} \tag{10b}$$

$$\bar{\alpha} = \sum_{i=1}^{3} p_i \alpha_i \tag{10c}$$

where p_i are known as the probabilities of the eigenvalue λ_i and α_1 is the averaged scattering angle corresponding to eigenvector i. The scattering entropy *H*, ranging between 0 and 1, quantifies the randomness of the scattering, whereas the anisotropy *A* (also bounded in [0,1]) indicates the relative contribution of the scatetring mechanism (eignvalues). The α identifies dominant scattering type, with values ranging from 0° (surface scattering) to 90° (double-bounce scattering), while intermediate values typically associated with volume scattering [34]. In other words, *H* and *A* characterize the heterogeneity of the scattering process, and the $\bar{\alpha}$ angle indicates the type of scattering mechanism. Results were visualised as (i) individual maps of *H*, *A* and $\bar{\alpha}$, (ii) an H–α plane following [24] and [35], and (iii) an HSV composite image in which Hue encodes $\bar{\alpha}$ (normalised 0–90°), Saturation encodes *H*, and Value encodes the Span [36]. The HSV provided a single integrated representation of scattering mechanism type, randomness and intensity across the scene, while the Cloude-Pottier classification (H–α plane) provided an unsupervised classification scheme to identify average scattering mechanisms.

7. RVI

Finally, RVI was computed to map the spatial pattern of vegetated and non-vegetated areas across the study area. SAR backscatter is highly sensitive to the geometric and dielectric properties of vegetation [37]. Accordingly, vegetation indices derived from SAR serve as a proxy for volume scattering and plant growth, providing a surrogate measure of vegetation condition. This study applied the quad-pol RVI [38], as follows:

$$RVI = \frac{8 \cdot \sigma^0_{HV}}{\sigma^0_{HH} + 2 \cdot \sigma^0_{HV} + \sigma^0_{VV}} \tag{11}$$

III. RESULTS

A. Pauli decomposition

From Fig. 3, differences in backscatter intensity across the Pauli components and HH, HV, VH, and VV channels reflect the diversity of surface targets within the scene. This is evident in the HH and VV channels (Fig. 3). The Pauli RGB composite provides an initial qualitative characterisation of dominant scattering mechanisms across the study area. Yellow tones, indicative of a mixture of double-bounce and volume scattering (strong red and green contributions), dominate the forested areas of Majete Wildlife Reserve (A) and Lengwe National Park (B). This is consistent with P-band penetration into woody canopies generating complex canopy-trunk and canopy-ground interactions [23]. The Elephant Marsh wetland (C) appears predominantly dark to dark-blue, interspersed with brownish-reddish patches. This generally reflects low total backscatter over open water and emergent vegetation with predominantly single-bounce or specular return and double-bounce interaction. The Nchalo Illovo Sugar Estate cropland (D) shows a patchy, high-contrast pattern of yellow, red and green tones corresponding to variable double-bounce and volume scattering from sugarcane fields. Notably, the sugarcane fields are resolved as distributed targets. Here, their dense, hectare-scale canopy produced a strong, polarimetric response across the cultivated fields. This demonstrates a potential agricultural application of Biomass P-band. The Shire (E) and Mwanza (F) rivers appear as narrow dark features, consistent with specular reflection and near-zero cross-pol returns over smooth water surfaces. The highland terrain to the northeast, including the area around Blantyre city (G), displays bright blue-white tones indicative of strong single-bounce and mixed scattering from steep topographic facets and urban structures.

Broadly, the co-polarised HH and VV channels show similar spatial patterns and intensity ranges (HH: mean −10.37, max 28.42 dB; VV: mean −11.23, max 28.15 dB). The cross-polarised HV channel returns substantially lower backscatter (mean −20.21, max 11.91 dB), approximately 10 dB below the co-pol mean as expected. Forested areas return moderate to high backscatter across all channels. In contrast, the water targets (river, dams) features appear as persistent low-backscatter regions, particularly in the VV channel. The sugarcane fields are clearly delineated as bright rectangular patches, particularly in HV channel. The Span image (mean −5.50, max 31.30 dB) provides the clearest land cover discrimination, integrating contrasts across all four channels. Horizontal banding artefacts are visible in HV but absent in HH, VV and Span, suggesting their confinement to the cross-polarisation channels.

This manuscript is a non-peer-reviewed EarthArXiv preprint that has been submitted to the IEEE Journal of Selected Topics in Applied Earth Observations and Remote Sensing. Subsequent versions may contain slightly different content.

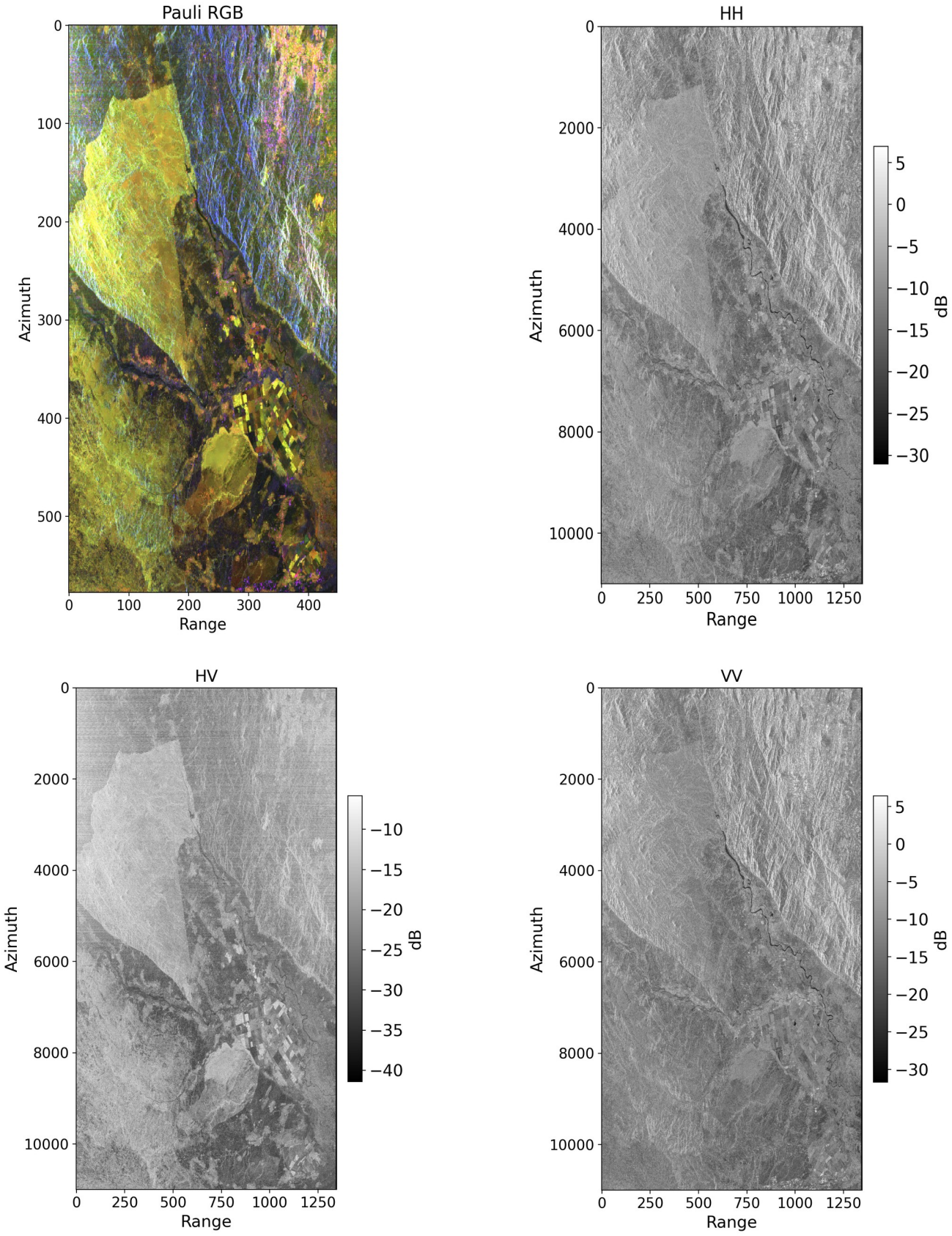

This manuscript is a non-peer-reviewed EarthArXiv preprint that has been submitted to the IEEE Journal of Selected Topics in Applied Earth Observations and Remote Sensing. Subsequent versions may contain slightly different content.

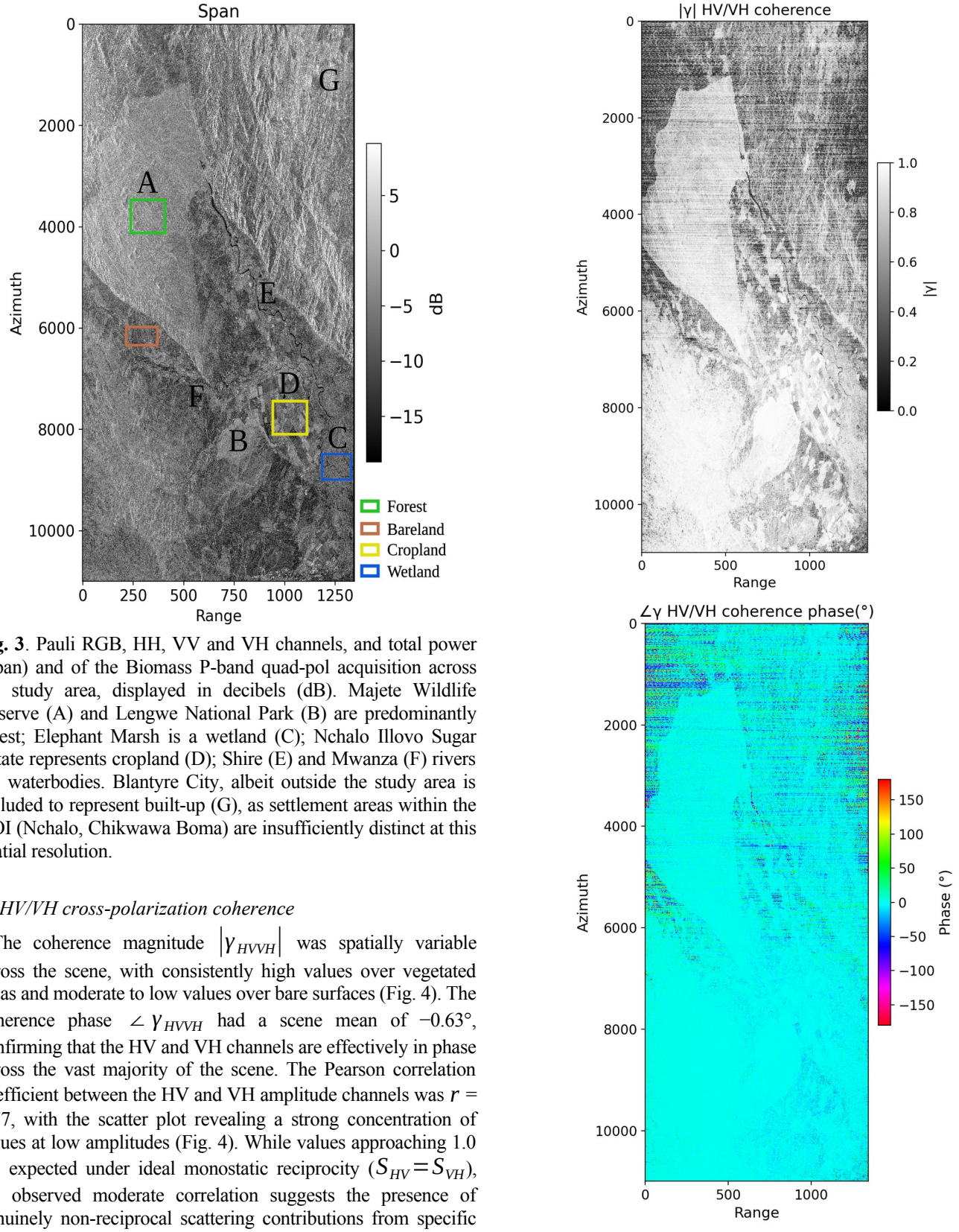

Fig. 3. Pauli RGB, HH, VV and VH channels, and total power (Span) and of the Biomass P-band quad-pol acquisition across the study area, displayed in decibels (dB). Majete Wildlife Reserve (A) and Lengwe National Park (B) are predominantly forest; Elephant Marsh is a wetland (C); Nchalo Illovo Sugar Estate represents cropland (D); Shire (E) and Mwanza (F) rivers are waterbodies. Blantyre City, albeit outside the study area is included to represent built-up (G), as settlement areas within the AOI (Nchalo, Chikwawa Boma) are insufficiently distinct at this spatial resolution.

B. HV/VH cross-polarization coherence

The coherence magnitude $|\gamma_{HVVH}|$ was spatially variable across the scene, with consistently high values over vegetated areas and moderate to low values over bare surfaces (Fig. 4). The coherence phase $\angle\gamma_{HVVH}$ had a scene mean of −0.63°, confirming that the HV and VH channels are effectively in phase across the vast majority of the scene. The Pearson correlation coefficient between the HV and VH amplitude channels was r = 0.77, with the scatter plot revealing a strong concentration of values at low amplitudes (Fig. 4). While values approaching 1.0 are expected under ideal monostatic reciprocity ($S_{HV} = S_{VH}$), the observed moderate correlation suggests the presence of genuinely non-reciprocal scattering contributions from specific target types within the scene or other factors beyond the scope of this study. This corroborates the spatial pattern observed in the coherence magnitude map.

This manuscript is a non-peer-reviewed EarthArXiv preprint that has been submitted to the IEEE Journal of Selected Topics in Applied Earth Observations and Remote Sensing. Subsequent versions may contain slightly different content.

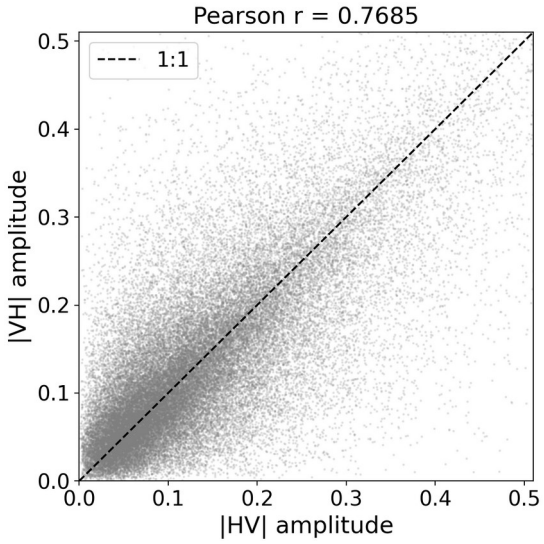

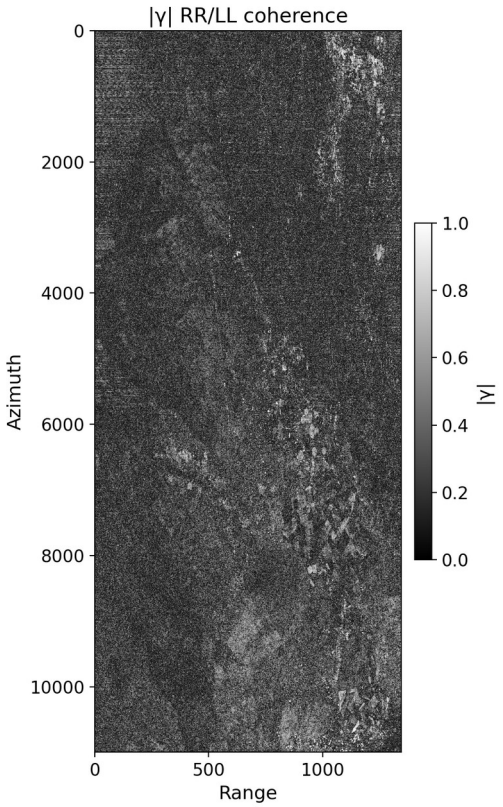

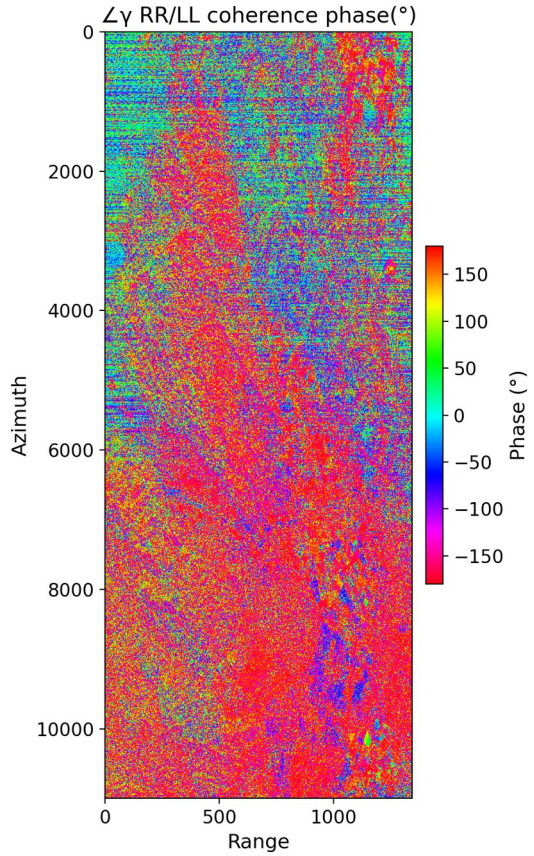

Fig. 4. Coherence magnitude $|\gamma|$ and phase $\angle\,\gamma$ of cross polarization channels HV and VH.

C. RR/LL circular polarization coherence

The mean RR/LL coherence magnitude across the scene was 0.29, substantially lower than the HV/VH coherence. Interestingly, this is physically consistent with the dominance of depolarising distributed targets, principally vegetation, across the study area. The coherence phase map $\angle\,\gamma_{RRLL}$ showed a broadly random distribution across the full ±180° range over vegetated areas, with a scene mean of −6.48° (std = 125.97°). This confirms the dominance of randomly oriented distributed scatterers. Distinct spatial patterns are nevertheless apparent. Notably, bare surfaces and river channel phase values close to 0° (green tones, Fig. 5), consistent with an orientation angle $\theta \approx 0°$. This is expected for surface scatterers [31]. By contrast, vegetated areas (forest, cropland and wetland) show a broad random phase distribution of mixed red and blue tones, reflecting the depolarising character of volume scatterers and randomly oriented canopy elements. These observations are consistent with the expected relationship $\angle\,\gamma_{RRLL} \approx 4\theta$ [31]. The Pearson correlation coefficient between the RR and LL amplitude channels was substantially low ($r = 0.46$). This agrees with the low coherence magnitude and confirms the pronounced RR/LL incoherence.

This manuscript is a non-peer-reviewed EarthArXiv preprint that has been submitted to the IEEE Journal of Selected Topics in Applied Earth Observations and Remote Sensing. Subsequent versions may contain slightly different content.

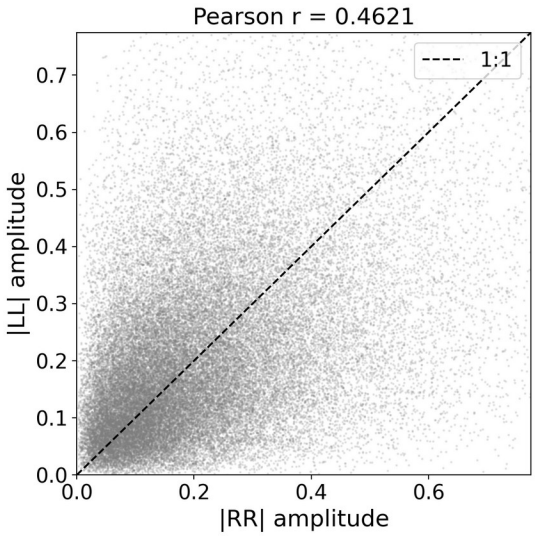

Fig. 5. Coherence magnitude $|\gamma|$ and phase $\angle\,\gamma$ between the RR and LL co-polarized channels.

D. Van Zyl and Y4R decompositions

The Van Zyl and Y4R decomposition results are provided in Fig. 6. Both models show broad agreement in the surface scattering component, where extensive dark blue areas signify a regime of dominant odd-bounce reflection. Reasonably, this is attributable to bare soil or sparsely vegetated surfaces where the P-band signal reaches the ground with minimal canopy attenuation. This is most pronounced across the topographic slopes and high-relief terrain in the upper-right of the scene. The two decompositions show broadly consistent spatial patterns (Fig. 6). The main difference is that the Y4R shows more red (double-bounce) across forested and wetland areas. This is expected. The Y4R includes an orientation angle compensation step and a helix scattering component to account for non-reflection-symmetric scattering. As noted by [28], in forested and wetland environments, such asymmetry arises from oriented canopy elements such as branches and trunks, which violate the reflection symmetry assumption of the Van Zyl model, as is the case here.

Interestingly, forest and non-forest boundaries are clearly delineated. For instance, the dense woodland and shrubland of Majete Wildlife Reserve in the upper-left of the scene is immediately visible. Evidently, surrounded by open terrain. In addition, the sugarcane plantation at Nchalo Estate is similarly well-defined, with high volume returns that contrast sharply against the surrounding surfaces. The wetland, by contrast, requires closer inspection to distinguish from adjacent bare and low-vegetation surfaces. Overall, this underscores the value of P-band imagery for forest delineation across the study area.

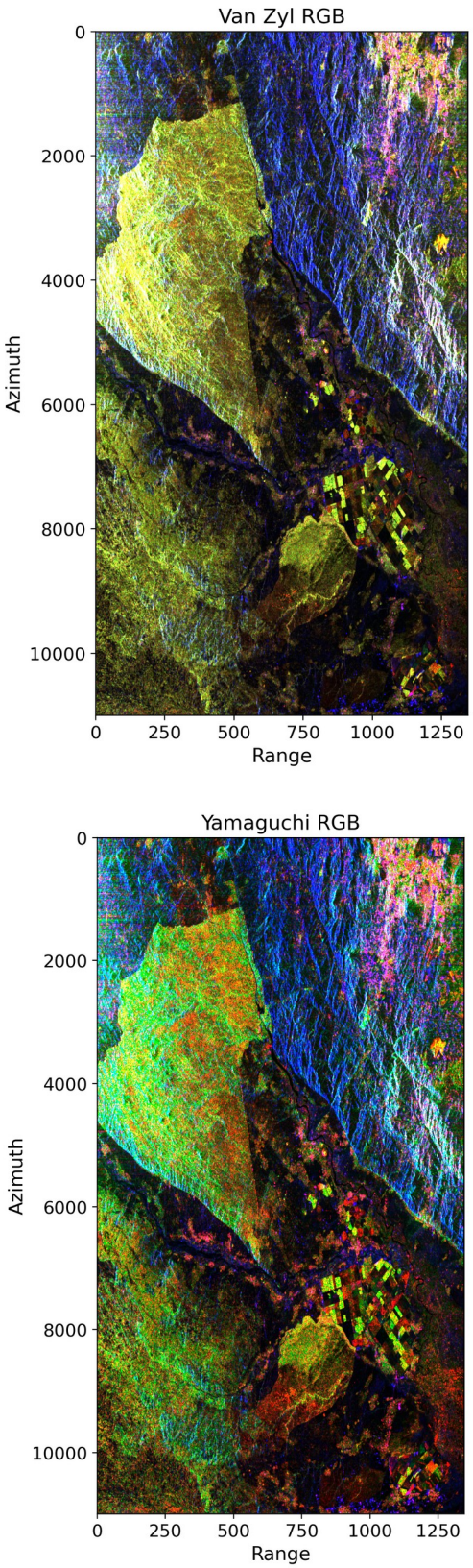

Fig. 6. Van Zyl and Yamaguchi Y4R polarimetric decomposition RGB composites (R = double-bounce, G = volume, B = odd/surface scattering).

This manuscript is a non-peer-reviewed EarthArXiv preprint that has been submitted to the IEEE Journal of Selected Topics in Applied Earth Observations and Remote Sensing. Subsequent versions may contain slightly different content.

E. H/A/$\bar{\alpha}$ decomposition and classification

The entropy map (Fig. 7a) reveals a spatially heterogeneous landscape (*H* mean = 0.58). High entropy areas (*H* > 0.8, light gray) dominate the vegetated areas. This indicates that multiple scattering mechanisms contribute comparably. Moderate entropy zones (*H* ~0.4-0.7, dark gray) represent a transitional regime between surface and volume scattering. Low entropy areas (*H* < 0.3, black) correspond to a single dominant scattering mechanisms, associated with specular surface reflection over calm water bodies and sparsely vegetated surfaces or bare land in the upper-right of the scene.

The anisotropy map (Fig. 7b) shows predominantly low values (*A* mean = 0.28) across the scene, appearing as dark gray. Such extensive dark gray areas of low anisotropy (*A* < 0.3) signify a regime where the secondary and tertiary eigenvalues are similar in magnitude ($\lambda 2 \approx \lambda 3$). Here, a low *A* value confirms one of the two hypothesis: a) either the presence of a single, purely dominant scattering mechanism ($\lambda 1$ only), as is evident in the topographic slopes and specular water bodies or b) completely depolarised behaviour as for the forested areas. The sparse light gray clusters visible in the central and upper-right portions of the map indicate that $\lambda 2 \gg \lambda 3$. In these areas, the scattering process is characterized by two distinct, dominant mechanisms (here, within the resolution cell).

The mean alpha angle map (Fig. 7c) shows that $\bar{\alpha}$ angle values across the scene predominantly range from 0° to 30° (dark blue to blue tones), consistent with a scene-wide mean of 25.92°. Moderate values (~40–60°, cyan-yellow) are spatially associated with the forested areas of Majete and Lengwe, the sugarcane plantation and the wetland. Of note, no strong double-bounce signature (red tones) are apparent in the mean alpha map. The H–α plane (Fig. 7e) confirms this, showing a continuous distribution moving from low entropy/low alpha toward high entropy at moderate alpha.

The dominant alpha angle map (Fig. 7d) shows surface scattering ($\alpha_1 \approx 0°$, dark blue) dominating the majority of the scene. Moderate values (cyan–green, ~40–50°) over the cropland, wetland and forested hillslopes indicate a transition toward volume scattering. Of note, parts of the sugarcane fields, escarpment and settlement area show the highest α_1 values (yellow–red, >60°), with localised pixels approaching 90°, indicating strong double-bounce. The H–α plane confirms a landscape dominated by surfaces covered by random media scattering. Interestingly, double-bounce contributions (α>80°) are sparse.

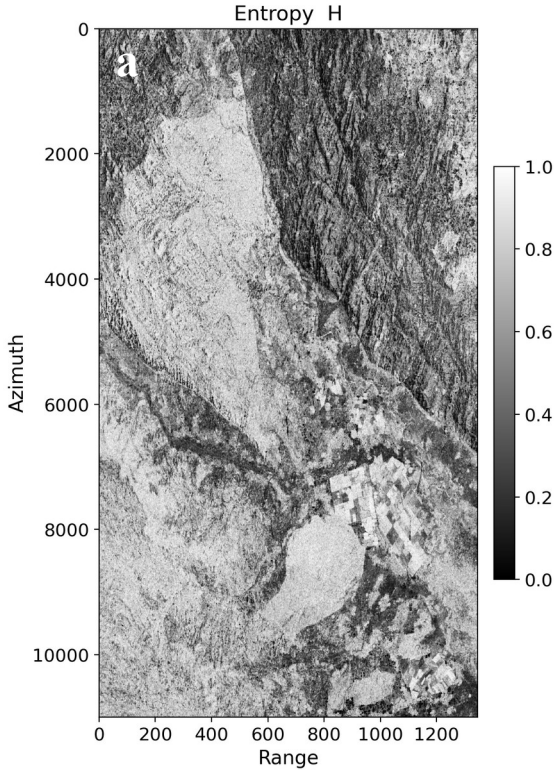

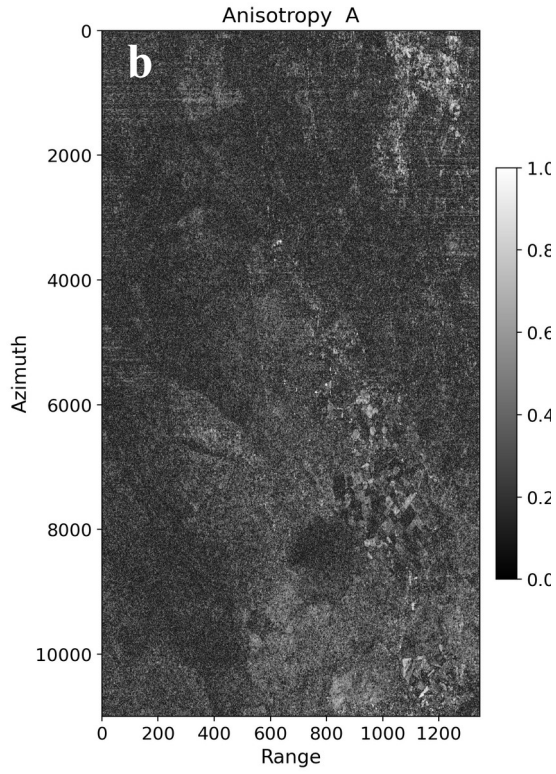

This manuscript is a non-peer-reviewed EarthArXiv preprint that has been submitted to the IEEE Journal of Selected Topics in Applied Earth Observations and Remote Sensing. Subsequent versions may contain slightly different content.

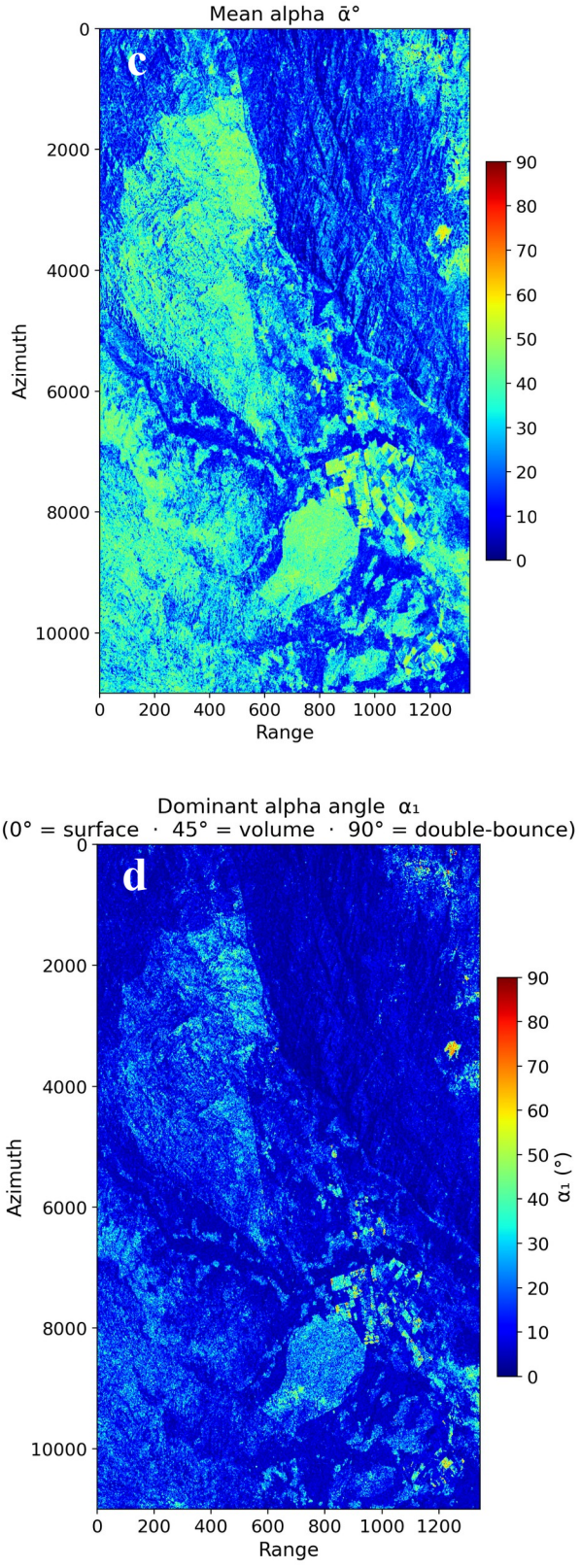

Fig. 7. The H/A/$\bar{\alpha}$ decomposition and Cloude-Pottier classification (H–α plane) Overall, the classification results are well matched with the Pauli and Span images above. A note on interpretation: entropy describes the degree of randomness in the scattering process, ranging from 0 (a single dominant scatterer) to 1 (multiple, random scattering mechanisms). In the H–α plane, zone 1 corresponds to a a quasi-deterministic dihedral reflector ($\alpha > 50°$, $H < 0.5$), representing double-bounce scattering (e.g., from trunk-ground and ground-building interactions). Zone 2 identifies quasi-deterministic dipole scattering ($40° < \alpha \leq 50°$, $H < 0.5$), typically associated with volume diffusion in oriented vegetation structures. Zone 3 represents quasi-deterministic Bragg surface ($\alpha \leq 40°$, $H < 0.5$), characteristic of calm water or smooth soil. Zone 4 denotes medium entropy double-bounce scattering ($\alpha > 50°$, $0.5 \leq H \leq 0.9$). Zone 5 ($40° \leq \alpha \leq 50°$, $0.5 \leq H \leq 0.9$) indicates medium entropy (moderately random) anisotropic scattering (vegetation canopy), while zone 6 identifies random surface scattering. The high entropy zones ($H \geq 0.9$, highly random) comprise 7 (complex multiple scattering), zone 8 (random anisotropic scattering), and zone 9 (non-feasible quadrant) where low alpha angles are mathematically incompatible with high randomness [24], [34].

The HSV composite (Fig. 8) provides a simultaneous interpretation of scattering type, randomness and intensity. The forested areas appear in (bright saturated) green-yellow tones, resulting from moderate alpha (~25–35°, green hue), high entropy (saturated colours) and relatively high Span (bright). The wetland displays cyan tones, reflecting slightly lower alpha (~15–25°, yellow-green hue), moderate entropy and moderate Span. The riverbanks, escarpment and highland terrain appear in gray, indicating low entropy (desaturated) with moderate Span. The sugarcane fields distinctly appear in bright saturated blue. This reflects moderate alpha and high entropy against high Span, consistent with structured double-bounce and volume interactions. Rivers and smooth water surfaces appear dark across the scene due to low Span. Overall, the HSV composite provides a visually intuitive land

This manuscript is a non-peer-reviewed EarthArXiv preprint that has been submitted to the IEEE Journal of Selected Topics in Applied Earth Observations and Remote Sensing. Subsequent versions may contain slightly different content.

cover discrimination, complementing the individual H/A/$\bar{\alpha}$ maps.

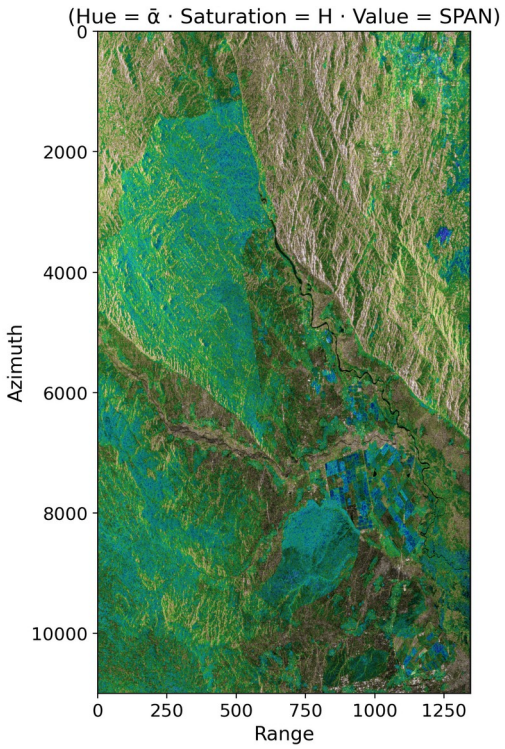

Fig. 8. HSV representation of H, $\bar{\alpha}$ and Span.

F. RVI

Fig. 9 presents RVI map, revealing vegetated and non-vegetated areas. Higher RVI values correspond to densely vegetated areas (shown in green), typical of landcover with significant biomass (here, forest and mature sugarcane field with peak biomass) In contrast, low RVI areas indicate non-vegetated surfaces, such as water bodies and bare soil (shown in white). For example, across the sugarcane fields, low RVI values indicate harvested fields, early plant emergence or land preparation conditions. Mean RVI was 0.4, indicating a heterogeneous landscape.

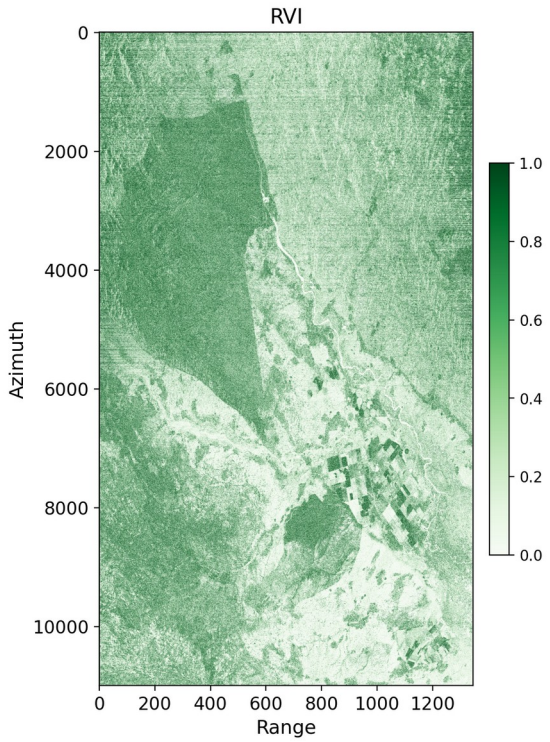

Fig. 9. RVI estimation showing vegetated and non-vegetated across across the study area. Higher values (darker green) indicate a high density of vegetation or increased biomass, while low values signify non-vegetated surfaces.

G. Landcover-specific polarimetric characterisation

An analysis was performed on four land cover sites selected to represent the main landscape types across the region: forest, wetland, cropland and bareland (Table 2). Here, the aim is to evaluate the extent to which the H/A/$\bar{\alpha}$ parameters discriminate between ecologically and physically distinct surface types.

TABLE 2

SUMMARY OF THE SITES.

Site	Landcover	Optical imagery
Forest (Majete Wildife Reserve)	Mixed savanna and miombo woodlands	

This manuscript is a non-peer-reviewed EarthArXiv preprint that has been submitted to the IEEE Journal of Selected Topics in Applied Earth Observations and Remote Sensing. Subsequent versions may contain slightly different content.

Wetland (Elephant Marsh)	Wetland, mosaic of rooted and floating vegetation	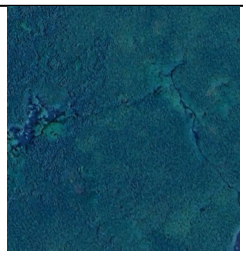
Cropland (Nchalo Sugar Estate)	Irrigated sugarcane	
Bareland (Chadzuka Village)	Bare soil, open terrain	

H. H/A/$\bar{\alpha}$ decomposition and classification

Table 3 presents the computed H/A/$\bar{\alpha}$ statistics for each site. Entropy is moderate-to-high across all vegetated sites, with means ranging from 0.684 (wetland) to 0.724 (forest), with cropland at 0.707. Bareland returns the lowest mean entropy (H = 0.516), consistent with a more deterministic surface scattering regime. Forest entropy is highest, reflecting the structural complexity of the closed woodland canopy. Anisotropy is broadly similar across all sites, with mean values ranging from 0.23 (forest) to 0.33 (wetland and cropland), and bareland at 0.27.

Mean alpha values are almost similar across the three vegetated sites: 33.18° (forest), 32.73° (wetland) and 33.74° (cropland), all clustering within the vegetation scattering regime (~20–45°). Bareland returns a substantially lower mean alpha (20.87°), consistent with dominant surface scattering. Cropland shows the widest spread ($\bar{\alpha}$ = 8.08°–62.67°), reflecting the heterogeneous mix of growth stages and bare soil patches across Nchalo Estate. Wetland has the highest maximum (63.34°), with isolated pixels approaching the double-bounce regime, suggesting localised vegetation-water interactions.

The dominant alpha angle α_1 reveals that the primary per-pixel scattering mechanism is consistently within the surface regime across all sites: 13.13° (forest), 16.24° (wetland), 15.92° (cropland) and 7.22° (bareland). The elevated mean alpha values are therefore driven by secondary and tertiary eigenvectors rather than the dominant mechanism. Cropland shows the widest spread in α_1 (std = 12.60°), indicating that double-bounce is the dominant mechanism in a subset of pixels. This seems consistent with cultivated land, where varying growth stages (planting, growing, maturing and harvesting) and land preparation give rise to a range of scattering mechanisms. Bareland has the most constrained distribution, confirming near-uniform surface scattering.

Taken together, all vegetated sites are high-entropy multi-mechanism scatterers occupying the volume scattering zone of the H–α plane (Fig. 10). Forest is structurally the most uniform, with high H, low A and a tightly bounded α_1. Wetland is distinguished by its extremes: the highest A and $\bar{\alpha}$ maxima. This points to localised double-bounce from vegetation-water interactions. Cropland is the most heterogeneous across every parameter. Bareland is clearly separable from the vegetated sites through its lower H, lower $\bar{\alpha}$ and markedly lower α_1, underscoring the value of P-band polarimetry for land cover discrimination.

TABLE 3
COMPUTED H/A/$\bar{\alpha}$ STATISTICS PER SITE.

Site	Parameter	Mean	Std Dev	Min	Max
Forest	H	0.72	0.15	0.09	0.99
	A	0.23	0.09	0.0	0.68
	$\bar{\alpha}$ (°)	33.18	9.83	2.98	58.71
	α_1 (°)	13.13	7.60	0.52	86.81
Wetland	H	0.68	0.13	0.11	0.96
	A	0.33	0.12	0.01	0.79
	$\bar{\alpha}$ (°)	32.73	9.72	6.14	63.34
	α_1 (°)	16.24	10.47	0.34	70.09
Cropland	H	0.71	0.17	0.17	0.99
	A	0.33	0.15	0.01	0.88
	$\bar{\alpha}$ (°)	33.74	11.89	8.08	62.67
	α_1 (°)	15.92	12.60	0.34	88.23
Bareland	H	0.52	0.16	0.10	0.95
	A	0.27	0.11	0.01	0.69
	$\bar{\alpha}$ (°)	20.87	8.31	4.29	50.27
	α_1 (°)	7.22	4.43	0.37	45.12

This manuscript is a non-peer-reviewed EarthArXiv preprint that has been submitted to the IEEE Journal of Selected Topics in Applied Earth Observations and Remote Sensing. Subsequent versions may contain slightly different content.

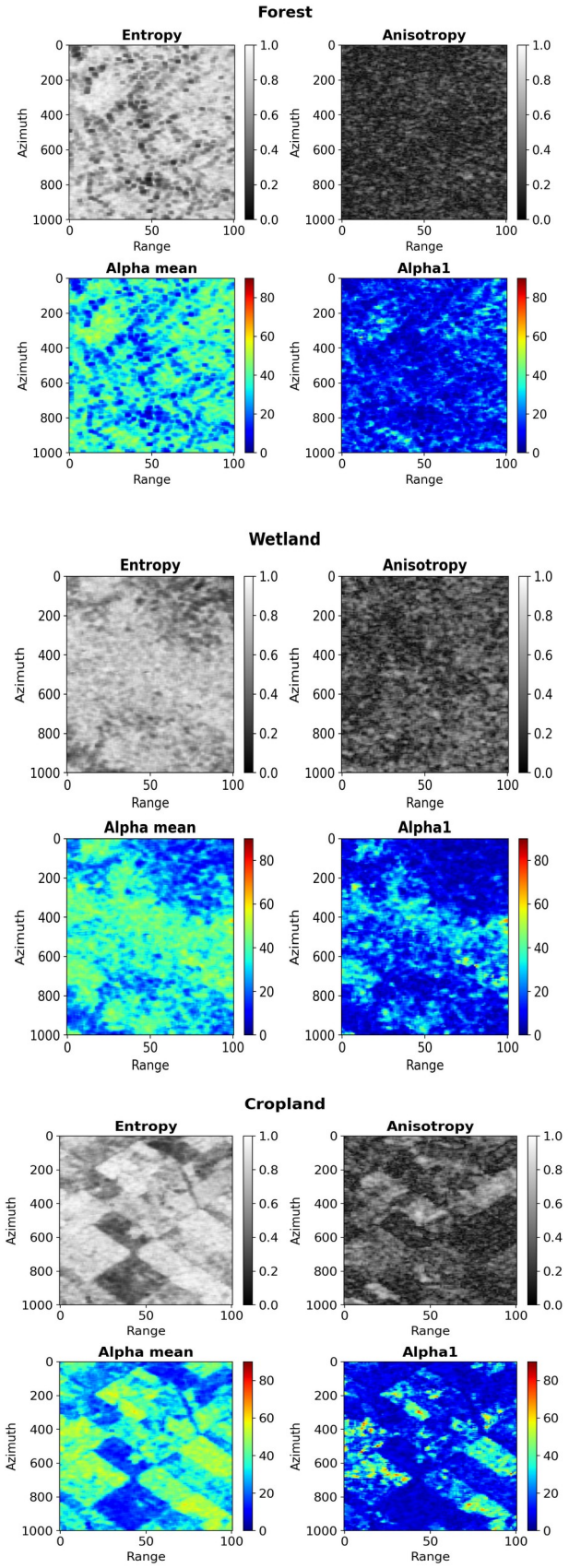

Fig. 10. Spatial distribution of H/A/$\bar{\alpha}$ decomposition parameters for the forest, wetland, cropland and bareland sites. Note, each site was extracted as a pixel bounding box from the full scene and processed independently through the coherency matrix formation and eigenvalue decomposition.

Fig. 11 below shows the H–α plane distributions for each land cover type. In forest, scattering mechanisms are concetrated in zones 5, 6 and 8, reflecting medium to high entropy anisotropic and random volume scattering. However, some points appear in zone 3, indicating surface scattering contributions from understory or forest floor exposure. In wetland, points span zones 3, 5, 6 and 8, indicating mixed surface, anisotropic, and random volume scattering. Notably, few points appear in zone 4, suggesting limited medium entropy double-bounce interactions. Similarly, cropland shows point distribution across zones 3-7. In contrast, bareland shows clustering mainly in zone 3, confirming quasi-deterministic Bragg surface scattering ($\bar{\alpha} \leq 40°$, $H < 0.5$) from smooth, exposed soil with minimal randomness. However, some points are observed in zone 6 (random surface scattering). This suggests noticeable heterogeneity within the bareland site, reasonably reflecting patches of vegetation. Overall, the presence of zone 3 points across all vegetated classes reflects P-band penetration to the ground surface, revealing underlying soil and water contributions even within forested and wetland areas.

This manuscript is a non-peer-reviewed EarthArXiv preprint that has been submitted to the IEEE Journal of Selected Topics in Applied Earth Observations and Remote Sensing. Subsequent versions may contain slightly different content.

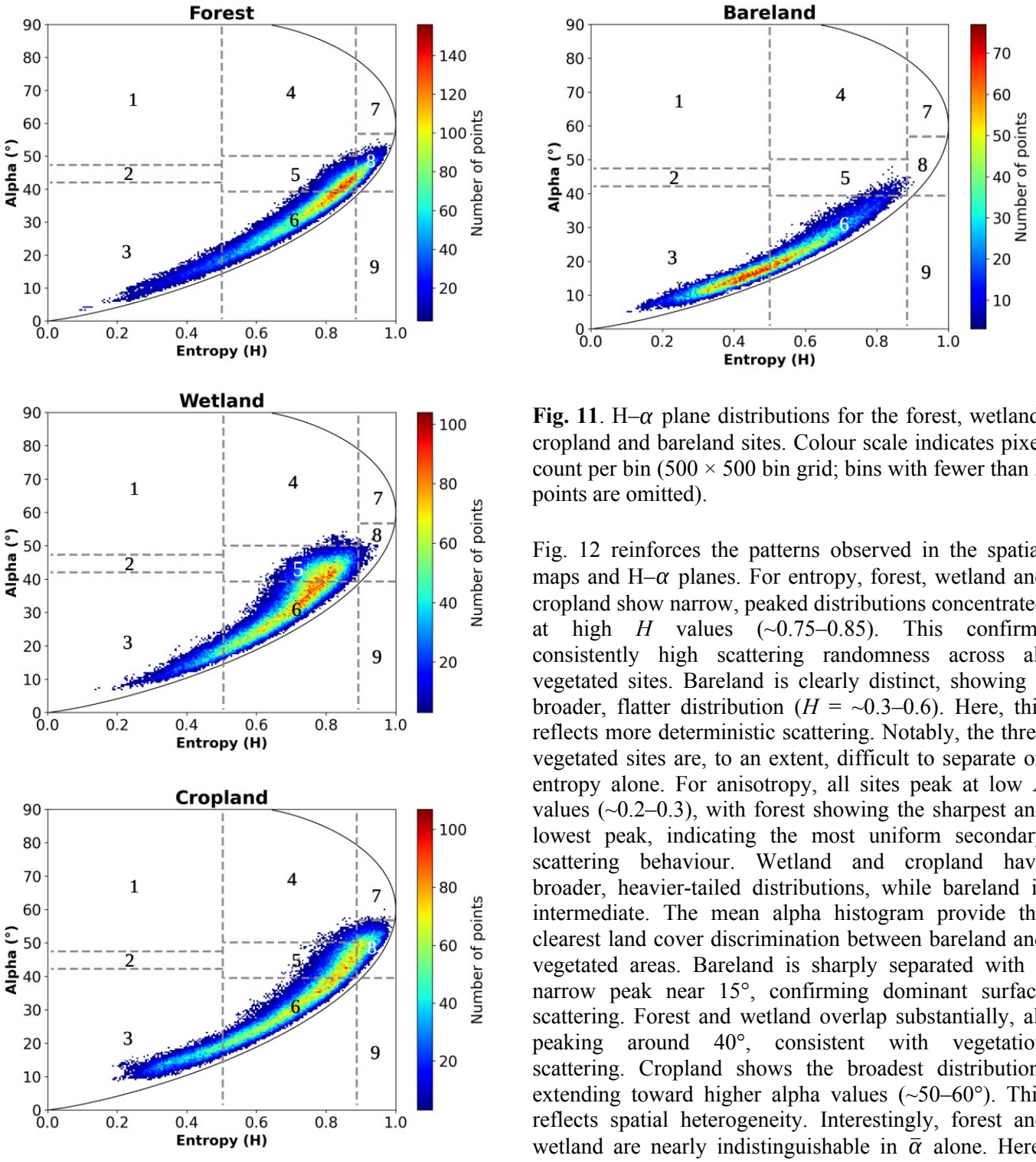

Fig. 11. H–α plane distributions for the forest, wetland, cropland and bareland sites. Colour scale indicates pixel count per bin (500 × 500 bin grid; bins with fewer than 3 points are omitted).

Fig. 12 reinforces the patterns observed in the spatial maps and H–α planes. For entropy, forest, wetland and cropland show narrow, peaked distributions concentrated at high H values (~0.75–0.85). This confirms consistently high scattering randomness across all vegetated sites. Bareland is clearly distinct, showing a broader, flatter distribution (H = ~0.3–0.6). Here, this reflects more deterministic scattering. Notably, the three vegetated sites are, to an extent, difficult to separate on entropy alone. For anisotropy, all sites peak at low A values (~0.2–0.3), with forest showing the sharpest and lowest peak, indicating the most uniform secondary scattering behaviour. Wetland and cropland have broader, heavier-tailed distributions, while bareland is intermediate. The mean alpha histogram provide the clearest land cover discrimination between bareland and vegetated areas. Bareland is sharply separated with a narrow peak near 15°, confirming dominant surface scattering. Forest and wetland overlap substantially, all peaking around 40°, consistent with vegetation scattering. Cropland shows the broadest distribution, extending toward higher alpha values (~50–60°). This reflects spatial heterogeneity. Interestingly, forest and wetland are nearly indistinguishable in $\bar{\alpha}$ alone. Here, the implication is that, $\bar{\alpha}$ cannot discriminate between forest and wetland, only between vegetated and non-vegetated.

This manuscript is a non-peer-reviewed EarthArXiv preprint that has been submitted to the IEEE Journal of Selected Topics in Applied Earth Observations and Remote Sensing. Subsequent versions may contain slightly different content.

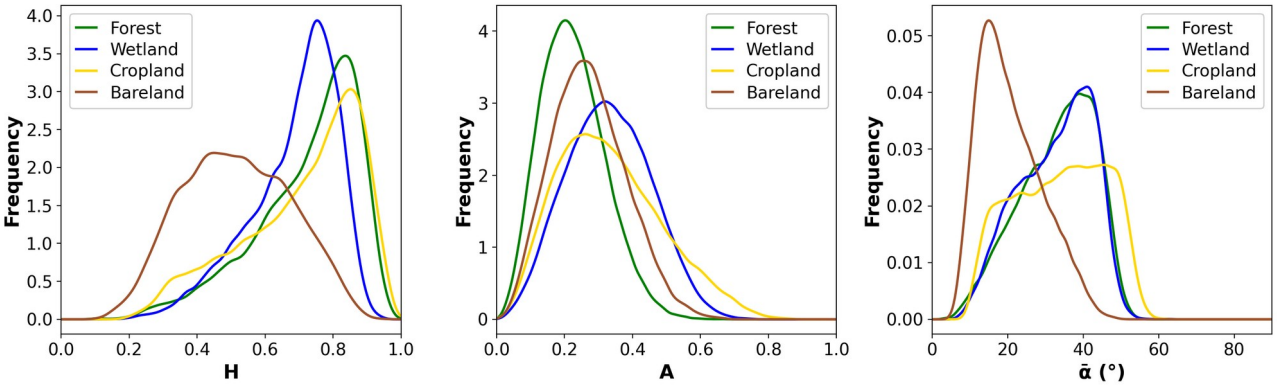

Fig. 12. Histograms of entropy, anisotropy and mean alpha angle across the four land cover sites.

I. Van Zyl and Y4R decompositions

The Van Zyl and Y4R RGB composites reveal spatially distinct scattering signatures across the four sites (Fig. 13). Over forest, both composites show a blue patches, reflecting surface scattering from sub-canopy penetration. Interestingly, the Van Zyl shows a notably darker red-brown background compared to Y4R. Here, sparse blue clusters throughout are consistent with P-band penetration to the ground layer, where the signal returns an odd-bounce component, a behaviour that would be attenuated at shorter wavelengths. Over wetland area, blue-green mixture dominates the scene, confirming volume and surface scattering as the primary mechanism. Of note, dark features correspond to open water channels. Of particular note is that the Y4R shows notably darker red-purple tones compared to Van Zyl. This is consistent with its redistribution of power from volume to double-bounce via the helix component. Such localised red patches indicate double-bounce returns typically associated with flooded vegetation. Again, this is generally a behaviour that would be absent at shorter wavelengths.

The cropland composite reveals a considerably heterogenous scene. Here, bright green, purple, blue and dark tones are arranged in a recognisable cultivated field pattern. The variation between parcels likely reflects diverse crop growth stages. Evidently, mature sugarcane canopies return volume scattering, while bare fields interact directly with the soil surface and early-growth fields allow P-band penetration through sparse vegetation, resulting in blue surface-dominant signatures instead. Purple and magenta tones indicate mixed double-bounce and surface returns, consistent with crop row geometry or field infrastructure. The Y4R shows more vivid green within individual parcels. The bareland composite is dominated by dark blue and near-black tones across both decompositions. This is consistent with the low backscatter and odd-bounce scattering expected from smooth, exposed soil. Scattered blue patches throughout the scene further confirm this signature. However, Y4R shows considerably more vivid green relative to the Van Zyl, suggesting a volume component not prominently by the later. Where the Y4R shows volume scattering, the Van Zyl instead returns localised double bounce. This reflects differences in how each component handles cross-polarization power and rotation effects, see López-Martínez and Pottier (2021).

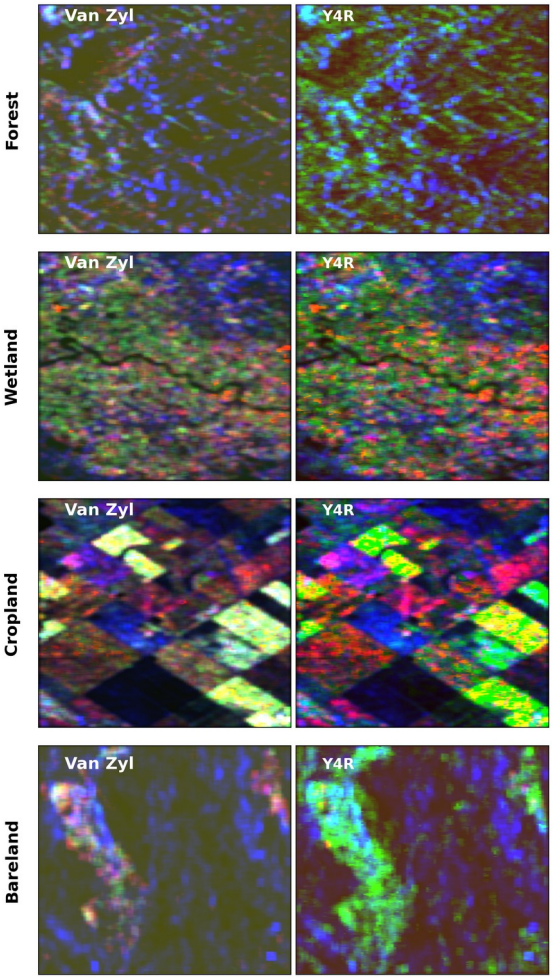

This manuscript is a non-peer-reviewed EarthArXiv preprint that has been submitted to the IEEE Journal of Selected Topics in Applied Earth Observations and Remote Sensing. Subsequent versions may contain slightly different content.

Fig. 13. Van Zyl and Y4R RGB composites for forest, wetland, cropland and bareland, illustrating site-specific P-band scattering mechanisms, sub-canopy penetration and vegetation density.

IV. Discussion

Based on application of SAR polarimetry on early-access Biomass P-band data, this study successfully extracted and decomposed polarimetric signatures on forest, cropland, wetland and bareland over the LSV floodplain. The derived parameters firmly show potential for novel applications in forest, cropland and wetland monitoring. The main finding is that surface scattering constitutes the dominant backscatter mechanism across the scene. This reflects both the prevalence of exposed soil within the floodplain mosaic, and the capacity of P-band wavelengths to penetrate vegetation canopies and interact with the underlying surface. Notably, even over the closed woodland canopies, the dominant alpha angle remains within the surface scattering regime. This means that backscatter originated mainly from the ground, confirming deep P-band penetration. This finding was clearly evident in the miombo woodlands (Fig. 10). This has direct implications for accurately separating soil and vegetation scattering model and carries clear benefits for (hectare-scale) above ground biomass estimation, vegetation classification and condition assessment, surface soil moisture retrieval, monitoring of water level under wetland vegetation, and the delineation of inundation [39]. Comparison of these findings with those of other studies [40] confirms that longer wavelengths penetrate larger biomass plants more effectively. And for smaller biomass vegetation, the penetration reaches the soil surface, resulting in dominant surface scattering contributions [39]. This lends further confidence to the interpretation that Biomass P-band is capable of separating larger from smaller biomass vegetation.

Volume scattering emerges as the second most significant contribution, most prominently across the forested areas at Majete Wildife Reserve and Lengwe National Park. Here, forest showed high volume returns that produced distinct signatures readily identifiable in both the Van Zyl and Y4R decomposition composites (see Figs. 6 and 13). Beyond forested areas, volume scattering was also detected over sugarcane plantations and dense wetland vegetation. Although the physical properties driving volume backscatter over sugarcane and dense wetland vegetation at P-band were not fully resolved in this study, it remains a compelling hypothesis that their density, spatial continuity, and elevated dielectric constant at the onset of the rainy season collectively contributed to the observed volume response. A dry-season comparison acquisition would be well-placed to test this. Double-bounce returns are sparse overall, confined principally to the built-up area.

Regarding land cover discrimination, entropy shows strong potential for separating forest, wetland, cropland and bare soils as a result of different physical properties. The alpha angle, meanwhile, excels at isolating bare soils from vegetated areas. However, it struggles to reliably distinguish forest from wetland. Hence, more studies are required to investigate land cover separability using H/A/α parameters. Anisotropy shows potential for finer intra-vegetation discrimination. However, its full diagnostic potential at P-band remains to be characterised, particularly with multi-temporal acquisitions. Of the linear polarizations, VV returns were consistent with specular reflections over calm water bodies, including the Shire River, as expected. Consistent with previous observations linking cross-polarization response to volume scattering from vegetation, the HV channel clearly identified forest and cropland better than HH and VV channels [40], [41].

Taken together, these results demonstrate that P-band penetrates forest, cropland and wetland vegetation and can discriminate dominant land cover types across a landscape characterized by a mix of complex composition, varying vegetation density, and diverse topography. We contend that these findings provide compelling scientific and operational motivation to begin developing forest and wetland inventories using Biomass P-band data. This is particularly relevant where shorter-wavelength SAR and optical data are limited, and once repeat acquisitions become available after the tomographic phase. Thus, further work is required to operationalise these findings in land and hydrological process modelling.

V. Conclusion

Prior to the Biomass mission, spaceborne P-band observations of vegetation structure and sub-canopy conditions over the floodplain were unavailable. The results presented here demonstrate that polarimetric decomposition of P-band data can discriminate between distinct land cover types across a heterogeneous floodplain mosaic, with entropy and mean alpha angle emerging as the most diagnostic parameters. This has direct relevance for the retrieval of key agricultural, hydrological, and forest parameters. Repeat observations spanning the full wet-dry seasonal cycle would permit assessment of how soil moisture, inundation extent, and vegetation phenology modulate the relative contributions of surface, volume, and double-bounce scattering. The approach presented is rigorous and readily implemented for new acquisitions. The integration of polarimetric decomposition parameters into a supervised classification framework represents a logical extension. This has the potential to map land cover and monitor anthropogenic change at the landscape scale.

Appendix

This manuscript is a non-peer-reviewed EarthArXiv preprint that has been submitted to the IEEE Journal of Selected Topics in Applied Earth Observations and Remote Sensing. Subsequent versions may contain slightly different content.

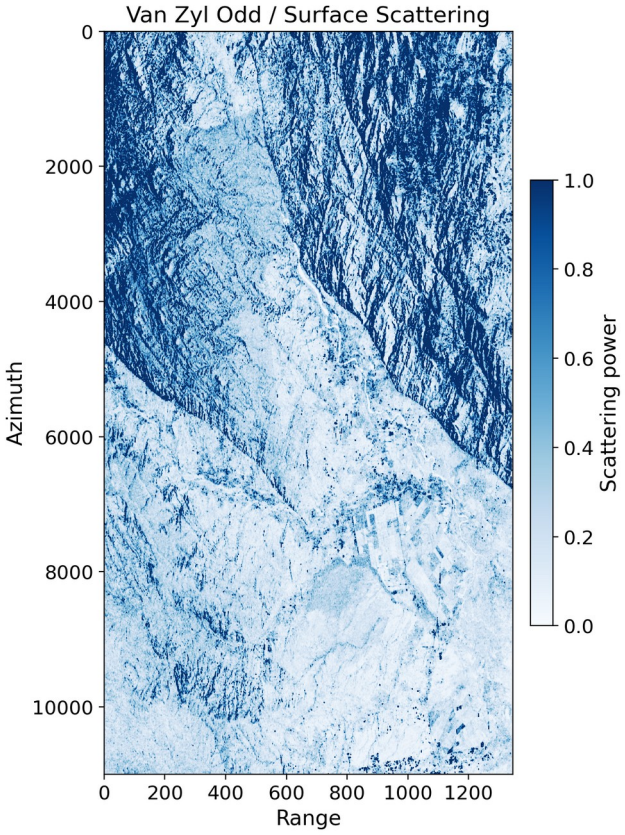

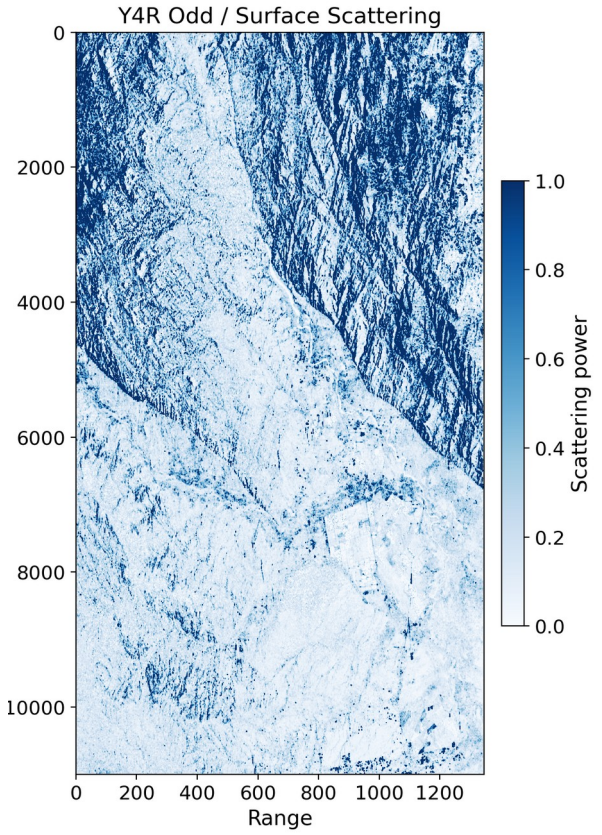

This manuscript is a non-peer-reviewed EarthArXiv preprint that has been submitted to the IEEE Journal of Selected Topics in Applied Earth Observations and Remote Sensing. Subsequent versions may contain slightly different content.

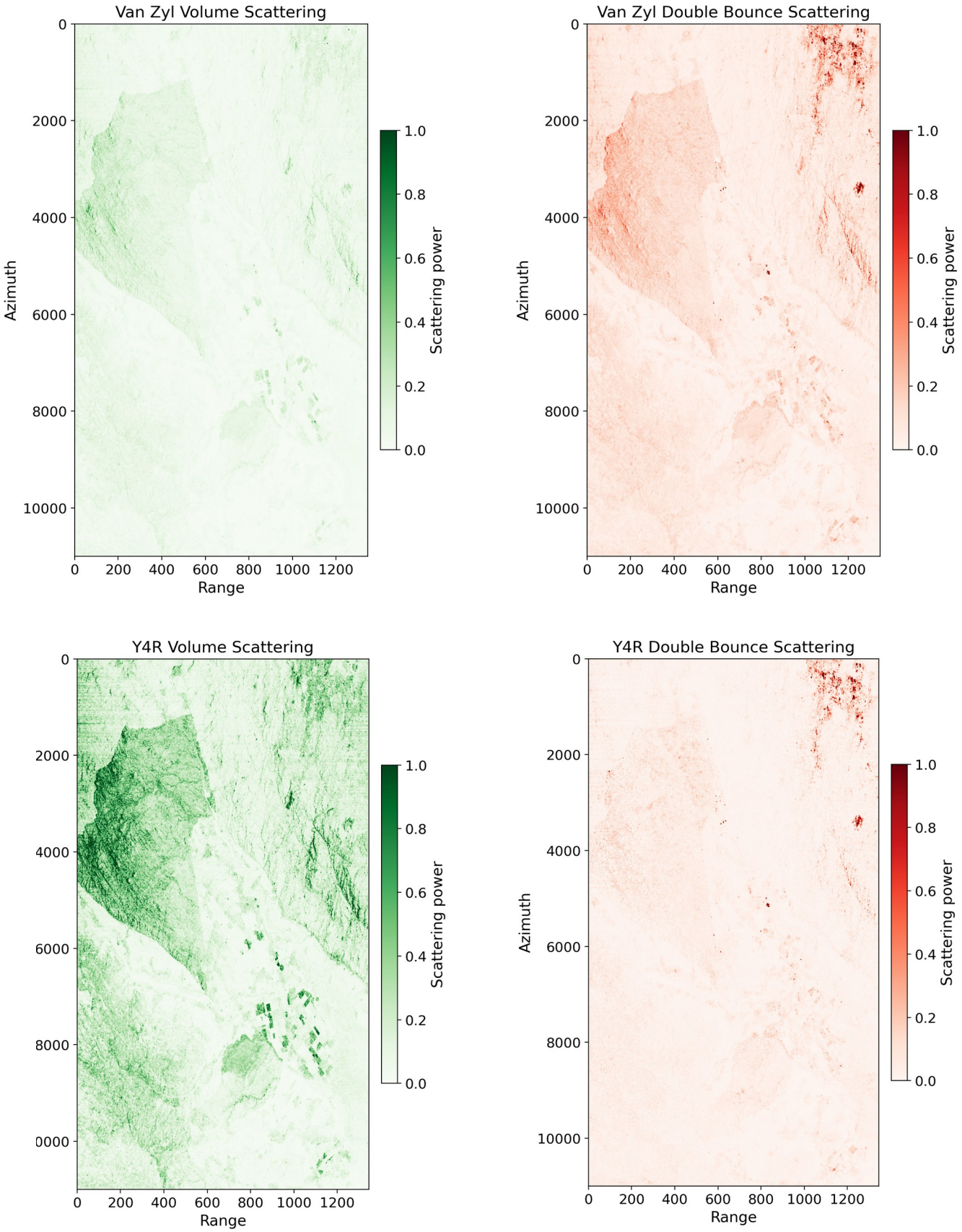

This manuscript is a non-peer-reviewed EarthArXiv preprint that has been submitted to the IEEE Journal of Selected Topics in Applied Earth Observations and Remote Sensing. Subsequent versions may contain slightly different content.

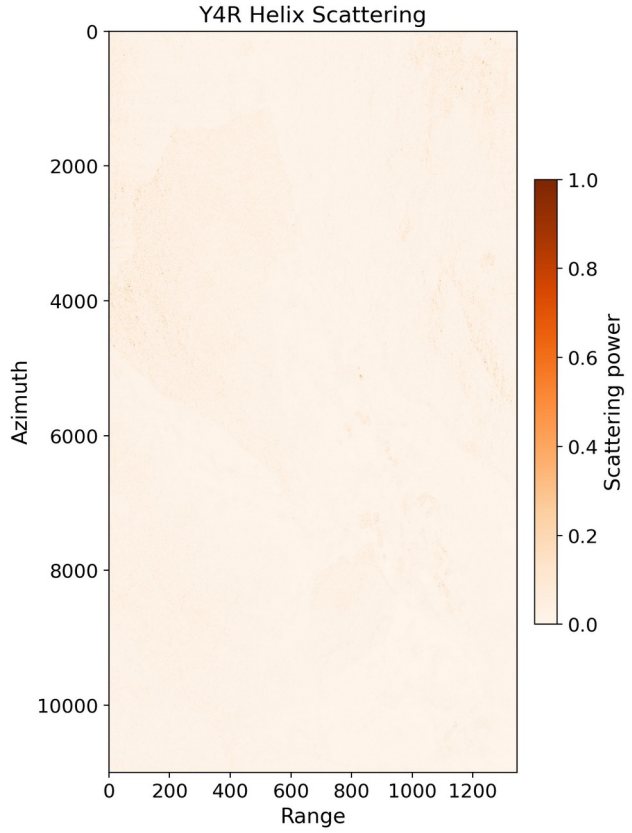

Fig. S1. The Van Zyl and Yamaguchi Y4R decomposition components across the study area: odd/surface, double-bounce, volume scattering, and helix (Y4R only). All components are normalised to a common 0–1 scale.

Acknowledgment

C.N. thanks the European Space Agency for providing training in Biomass accessing, processing and analysis through the 8th ESA Advanced Course on Radar Polarimetry 2026, held in Slovenia. The authors would like to thank the European Space Agency for providing open-access to the P-SAR data collected during Biomass campaign.

Conflict of Interest

None of the authors have a conflict of interest to disclose.

References

[1] Y. Zhu, K. Yoshimura, Y. Liu, and H. Fu, "Global flood extent monitoring using SAR satellite and hydrological data: A multi-scale and multi-source approach," Journal of Hydrology, vol. 663, pt. A, p. 134074, 2025.

[2] T. Dilip, M. Kumari, C. S. Murthy, et al., "Monitoring early-season agricultural drought using temporal Sentinel-1 SAR-based combined drought index," Environmental Monitoring and Assessment, vol. 195, p. 925, 2023.

[3] R. Sugimoto, S. Kato, R. Nakamura, C. Tsutsumi, and Y. Yamaguchi, "Deforestation detection using scattering power decomposition and optimal averaging of volume scattering power in tropical rainforest regions," Remote Sensing of Environment, vol. 275, p. 113018, 2022.

[4] S. J. Goetz, A. Baccini, N. T. Laporte, et al., "Mapping and monitoring carbon stocks with satellite observations: A comparison of methods," Carbon Balance and Management, vol. 4, p. 2, 2009.

[5] J. Arigony-Neto, F. Rau, H. Saurer, et al., "A time series of SAR data for monitoring changes in boundaries of glacier zones on the Antarctic Peninsula," Annals of Glaciology, vol. 46, pp. 55–60, 2007.

[6] A. C. Mondini, F. Guzzetti, K.-T. Chang, O. Monserrat, T. R. Martha, and A. Manconi, "Landslide failures detection and mapping using Synthetic Aperture Radar: Past, present and future," Earth-Science Reviews, vol. 216, p. 103574, 2021.

[7] European Investment Bank, "What is an ecosystem service?" 2023. [Online]. Available: https://www.eib.org/en/stories/ecosystem-service-nature

[8] African Development Bank and Global Environment Facility, "AfDB-GEF activity report: Integrating climate change and natural resources management for sustainable development in Africa," African Development Bank Group, 2022.

[9] A. Alonso-Robisco, J. M. Carbo, E. Kormanyos, and E. Triebskorn, "Houston, we have a problem: Can satellite information bridge the climate-related data gap?" Latin American Journal of Central Banking, 2026, doi: 10.1016/j.latcb.2025.100173.

[10] F. V. Sainuddin, S. Chirakkal, S. V. Asok, et al., "Evaluation of multifrequency SAR data for estimating tropical above-ground biomass by employing radiative transfer modeling," Environmental Monitoring and Assessment, vol. 195, p. 1102, 2023.

[11] FY. Bai, W. Wu, Z. Yang, J. Yu, B. Zhao, X. Liu, H. Yang, E. Mas, and S. Koshimura, "Enhancement of detecting permanent water and temporary water in flood disasters by fusing Sentinel-1 and Sentinel-2 imagery using deep learning algorithms: Demonstration of Sen1Floods11 benchmark datasets," Remote Sensing, vol. 13, no. 11, p. 2220, 2021.4.

[12] J. Liao, G. Shen, and L. Dong, "Biomass estimation of wetland vegetation in Poyang Lake area using ENVISAT advanced synthetic aperture radar data," Journal of Applied Remote Sensing, vol. 7, no. 1, p. 073579, 2013.. L. Imhoff, "Radar backscatter and biomass saturation: Ramification for global biomass inventory," IEEE Transactions on Geoscience and Remote Sensing, vol. 33, no. 2, pp. 511–518, 1995.

[13] PP. S. Bharadwaj, S. Kumar, S. P. S. Kushwaha, and W. Bijker, "Polarimetric scattering model for estimation of above-ground biomass of multilayer vegetation using ALOS-PALSAR quad-pol data," Physics and Chemistry of the Earth, vol. 83–84, pp. 187–195, 2015.

[14] J.M. P. F. Costa, O. Niemann, E. Novo, and F. Ahern, "Biophysical properties and mapping of aquatic vegetation during the hydrological cycle of the Amazon floodplain using JERS-1 and Radarsat," International Journal of Remote Sensing, vol. 23, no. 7, pp. 1401–1426, 2002.

[15] F. S. Marzano, "Radiative transfer theory," in Encyclopedia of Remote Sensing, E. G. Njoku, Ed. Springer, New York, NY, 2014.

[16] F. T. Ulaby, R. K. Moore, and A. K. Fung, Microwave Remote Sensing: Active and Passive. Artech House, 2014.

[17] M. L. Imhoff, "Radar backscatter and biomass saturation: Ramification for global biomass inventory," IEEE Transactions on Geoscience and Remote Sensing, vol. 33, no. 2, pp. 511–518, 1995.

[18] P. Ferrazzoli and L. Guerriero, "Radar sensitivity to tree geometry and woody volume: A model analysis," IEEE Transactions on Geoscience and Remote Sensing, vol. 33, no. 2, pp. 360–371, 1995.

[19] European Space Agency, et al., "Biomass level 1A," ver. 1.0, European Space Agency, 2025.

[20] O. D'Hondt, "Python PolSARpro: A re-implementation of selected PolSARpro functions in Python following the scientific recommendations of PolInSAR 2021," Apache License 2.0, 2026. [Online]. Available: https://github.com/satim-co/PolSARpro

[21] Global Forest Watch, "Chikwawa, Malawi deforestation rates & statistics," 2025. [Online]. Available: https://www.globalforestwatch.org/dashboards/country/MWI/3/

[22] D. Zanaga, R. Van De Kerchove, D. Daems, et al., "ESA WorldCover 10 m 2021 v200," 2022, doi: 10.5281/zenodo.7254221.

[23] DLR, "Raise the curtain as BIOMASS takes centre stage – Earth's 'lung volume detector'," 2025. [Online]. Available: https://www.dlr.de/en/latest/news/2025/raise-the-curtain-as-biomass-takes-centre-stage-earths-lung-volume-detector

[24] S. R. Cloude and E. Pottier, "A review of target decomposition theorems in radar polarimetry," IEEE Transactions on Geoscience and Remote Sensing, vol. 34, no. 2, pp. 498–518, 1996.

This manuscript is a non-peer-reviewed EarthArXiv preprint that has been submitted to the IEEE Journal of Selected Topics in Applied Earth Observations and Remote Sensing. Subsequent versions may contain slightly different content.

[25] J. J. Van Zyl, "Unsupervised classification of scattering mechanisms using radar polarimetry data," IEEE Transactions on Geoscience and Remote Sensing, vol. 27, no. 1, pp. 36–45, 1989.
[26] Y. Yamaguchi, T. Moriyama, M. Ishido, and H. Yamada, "Four-component scattering model for polarimetric SAR image decomposition," IEEE Transactions on Geoscience and Remote Sensing, vol. 43, no. 8, pp. 1699–1706, 2005
[27] J.-S. Lee and E. Pottier, Polarimetric Radar Imaging: From Basics to Applications, 1st ed. CRC Press, 2009.
[28] C. López-Martínez and E. Pottier, "Basic principles of SAR polarimetry," in Polarimetric Synthetic Aperture Radar, I. Hajnsek and Y.-L. Desnos, Eds. Springer, Cham, 2021, vol. 25, pp. 1–57.
[29] J.-S. Lee, T. L. Ainsworth, J. P. Kelly, and C. Lopez-Martinez, "Evaluation and bias removal of multilook effect on entropy/alpha/anisotropy in polarimetric SAR decomposition," IEEE Transactions on Geoscience and Remote Sensing, vol. 46, no. 10, pp. 3039–3052, 2008.
[30] J. J. Van Zyl and Y. Kim, "Basic principles of SAR polarimetry," in Synthetic Aperture Radar Polarimetry. Jet Propulsion Laboratory, National Aeronautics and Space Administration, 2011, pp. 17–80.
[31] T. L. Ainsworth, D. L. Schuler, and J. S. Lee, "Polarimetric SAR characterization of manmade structures in urban areas using normalized circular-pol correlation coefficients," Remote Sensing of Environment, vol. 112, no. 6, pp. 2876–2885, 2008.
[32] V. Alberga, E. Krogager, M. Chandra, and G. Wanielik, "Potential of coherent decompositions in SAR polarimetry and interferometry," in Proceedings of the 2004 IEEE International Geoscience and Remote Sensing Symposium (IGARSS), vol. 3, 2004, pp. 1792–1795.
[33] Y. T. Jung and S.-E. Park, "Comparative analysis of polarimetric SAR calibration methods," Remote Sensing, vol. 10, no. 12, p. 2060, 2018.
[34]. S. R. Cloude and E. Pottier, "An entropy based classification scheme for land applications of fully polarimetric SAR," IEEE Transactions on Geoscience and Remote Sensing, vol. 35, no. 1, pp. 68–78, 1997.
[35] L. Mascolo, et al., "Polarimetric SAR decomposition in random media," Remote Sensing, vol. 13, no. 5, p. 2024, 2024.
[36] C. Koyama, "PolSARpro tutorial notes," Center for Northeast Asian Studies, Tohoku University, 2016. [Online]. Available: http://cobalt.cneas.tohoku.ac.jp/users/sato/PolSARpro%20Tutorial%20Notes.pdf
[37] D. Ratha, D. Mandal, S. Dey, et al., "New vegetation indices for full and compact polarimetric SAR data: In preparation for the Radarsat constellation mission (RCM)," ISPRS Annals of the Photogrammetry, Remote Sensing and Spatial Information Sciences, vol. IV-3/W2-2020, pp. 41–48, 2020.
[38] D. Ryu and S.-G. Lee, "Mapping vegetation water content over agricultural landscapes using satellite C- and X-band synthetic aperture radar," in IGARSS 2023 - 2023 IEEE International Geoscience and Remote Sensing Symposium, 2023, pp. 399–402.
[39] J. M. Lopez-Sanchez, J. D. Ballester-Berman, F. Vicente-Guijalba, et al., "Agriculture and wetland applications," in Polarimetric Synthetic Aperture Radar, I. Hajnsek and Y.-L. Desnos, Eds. Springer, 2021, vol. 25.
[40] H. McNairn, J. Shang, X. Jiao, and C. Champagne, "The contribution of ALOS PALSAR multipolarization and polarimetric data to crop classification," IEEE Transactions on Geoscience and Remote Sensing, vol. 47, no. 12, pp. 3981–3992, 2009.
[41] J.-S. Lee, M. R. Grunes, and E. Pottier, "Quantitative comparison of classification capability: Fully polarimetric versus dual and single-polarization SAR," IEEE Transactions on Geoscience and Remote Sensing, vol. 39, no. 11, pp. 2343–2351, 2001.

Clinton NKolokosa (Student Member, IEEE) received the B.Sc. degree in natural resources management from Lilongwe University of Agriculture and Natural Resources, Lilongwe, Malawi, and the M.Sc. degree in geographic information systems from Sheffield Hallam University, Sheffield, U.K. He is currently pursuing the Ph.D. degree in Environmental Sciences at the University of Stirling, Stirling, U.K., as a Commonwealth Scholar. He is an Associate Fellow of the Royal Geographical Society with the Institute of British Geographers. His doctoral research pioneers the application of long-wavelength microwave remote sensing to the predictive mapping of freshwater habitats for schistosomiasis snail hosts, working at the precise intersection of Earth observation, ecology, climate change, and global health. Prior to his doctorate, he served as a Wellcome International Master's Fellow and a geospatial analyst at the Malawi-Liverpool-Wellcome Programme.

Olivier D'Hondt received the B.Sc. degree in electrical engineering from the University of Rennes 1, Rennes, France, in 2000, the M.Sc. degree in electrical engineering with a major in image processing from the University of Rennes 1 in 2002, and the Ph.D. degree in signal processing from the University of Rennes 1 in 2006. He is a Remote Sensing Data Scientist with over 15 years of expertise in developing advanced algorithms for satellite data analysis and Earth observation applications. From 2007 to 2021, he held research and engineering positions at the Barcelona Media Innovation & Research Center, Polytechnic University of Catalonia, and Technical University of Berlin, focusing on computer vision and remote sensing. In 2022, he served as Senior SAR Scientist at Floodbase, USA, specializing in synthetic aperture radar data processing. Since October 2023, he has been an open source developer for EO-Tools. His expertise encompasses Python, C++, and machine learning frameworks, with a strong background in image processing, synthetic aperture radar, and Earth observation applications.

Lucio Mascolo (Member, IEEE) was born in Italy, in 1983. He received the B.Sc. and M.Sc. degrees (summa cum laude) in telecommunications engineering from the Università degli Studi di Napoli Parthenope, Naples, Italy, in 2007 and 2011, respectively, and the Ph.D. degree in electronic and information engineering (curriculum electromagnetic fields) from the Università degli Studi di Cagliari, Cagliari, Italy, in 2015. From 2015 to 2016, he was a postdoc with the Electromagnetics and Remote Sensing Group, Università degli Studi di Napoli Parthenope. He was a researcher with with SarVision, Wageningen, The Netherlands, from 2016 to 2018, and with with Digital Content Analysis Technology, Glasgow, U.K., from 2019 to 2020. He has been a researcher in Spain since 2020, when he joined the Signals, Systems and Telecommunication Group at the University of Alicante, and then the Global Change Unit - Image processing Laboratory, University of Valencia in 2023. He is currently a researcher at Radarmetrics, in Santander. His research interests include radar remote sensing of the environment, polarimetric scattering models, estimation of geophyiscal variables, SAR

This manuscript is a non-peer-reviewed EarthArXiv preprint that has been submitted to the IEEE Journal of Selected Topics in Applied Earth Observations and Remote Sensing. Subsequent versions may contain slightly different content.

imaging techniques, and applications of SAR remote in agriculture and land monitoring.

Tiwonge Mzumara-Gawa received the M.Sc. degree in conservation biology from the University of Cape Town, Cape Town, South Africa, and the Ph.D. degree in ecological sciences from the University of KwaZulu Natal, Durban, South Africa. She is a Senior Lecturer in Ecology within the Biological Sciences Department at the Malawi University of Science and Technology, Lilongwe, Malawi. She leads the institutional consortium in Malawi developing the field of biodiversity informatics and has been instrumental in publishing Malawi's first datasets on the Global Biodiversity Information Facility website. She has over 10 years of experience in ecology and conservation projects, including species and biodiversity assessments across Malawi and coaching in Protected Area Management Effectiveness assessments. She is the current National Chairperson of the Wildlife and Environmental Society of Malawi.

Petros Chigwechokha received the Ph.D. degree in molecular biology from Kagoshima University, Kagoshima, Japan. He is a Senior Lecturer and the Head of the Department of Biological Sciences at Malawi University of Science and Technology, Thyolo, Malawi. A recombinant technologist by training, his research focuses on the application of genetics and molecular-based approaches to understanding aquatic biota, human life, and the environment, with particular emphasis on environmental and wastewater-based multi-pathogen detection through genomic approaches. His research interests extend to fish genetics, molecular ecology, phylogenetics, synthetic biology, and biosystem modulation to explore physiological protein functions in fish models. He has developed expertise in wastewater-based epidemiology and is currently involved in wastewater-multi-pathogen surveillance in resource-limited settings.

Russell Stothard received the B.Sc. degree in zoology and microbiology from the University of Leeds, Leeds, U.K., in 1991, the M.Sc. degree in biological computation from York University, York, U.K., in 1992, and the Ph.D. degree in biology from Imperial College London and the Natural History Museum, London, U.K., in 1995. He was awarded a Senior Fellowship of the Higher Education Academy in 2020 and is a Professor of Tropical Disease Biology and Medical Parasitology at the Liverpool School of Tropical Medicine, Liverpool, U.K., where he has been since 2011. He currently serves on the WHO Strategic Technical Advisory Group on Neglected Tropical Diseases, WHO Regional Expert Advisory Group on Urogenital Schistosomiasis, and as Editor-in-Chief of Parasitology (Cambridge University Press). He leads multidisciplinary research programs across Central, East, and West Africa, with long-term collaborations in Lake Malawi, Tanzania, Zanzibar, and Cameroon, adopting One Health approaches to investigate aquatic ecosystem health and sustainable management.

Zarah Pattison received the B.Sc. (Hons.) degree in ecology from Royal Holloway University of London, London, U.K., in 2011, the M.Res. degree in biological sciences by research from Royal Holloway University of London in 2012, and the Ph.D. degree in ecology from the University of Stirling, Stirling, U.K., in 2016, funded by Scottish Natural Heritage and the Scottish Environment Protection Agency. She is a Senior Lecturer in Plant Science with the Faculty of Biological and Environmental Sciences at the University of Stirling. Her research broadly focuses on the dispersal, impacts, and management of invasive non-native species in freshwater and forest environments, with particular interest in threats to water and food security, dispersal pathways, and habitat restoration. She has expertise in community and ecosystem responses to biological invasions and social perceptions of invasive species.

Armando Marino (Member, IEEE) received the M.Sc. degree in telecommunication engineering from the Universita' di Napoli "Federico II," Naples, Italy, in 2006, and the Ph.D. degree in polarimetric SAR interferometry from the School of Geosciences, University of Edinburgh, Edinburgh, U.K., in 2011. In 2006, he joined the High Frequency and Radar Systems Department, German Aerospace Centre, Oberpfaffenhofen, Germany, where he developed his M.Sc. thesis. From March 2011 to October 2011, he was with the Institute of Computing Research, University of Alicante, Alicante, Spain. From December 2011 to May 2015, he was a Postdoctoral Researcher and Lecturer with the Institute of Environmental Engineering, ETH Zurich, Zurich, Switzerland. From June 2015, he was a Lecturer with the School of Engineering and Innovation, Open University, Milton Keynes, U.K. Since May 2018, he has been an Associate Professor with the Faculty of Natural Sciences, University of Stirling, Stirling, U.K.